Direct Writing Techniques: Electron Beam and Focused Ion Beam

T. Djenizian and C. Lehrer

1 Introduction

Due to significant theoretical and technological new advances, nanostructuring of surfaces has attracted a great deal of scientific interest. The continuous demand for shrinking the dimensions of structures to reach the nanometer scale is mainly motivated by the discovery of new behaviors dominated by unique properties that are encountered when nanosize dimensions are approached (e.g., quantum confinement). Additionally, a major thrust for shrinking dimensions originates from the microelectronic field requiring the development of smaller devices, system integration, and system diversification. Thus, electronic materials as well as integrated materials adding new features must be structured at the micro- and nanometer scale.

Methods to locally micro- and nanostructuring surfaces have been intensively explored in recent years and have rapidly found technological applications. Most of these techniques are based on lithography and hence demand a masking process. To date, optical lithography is the main technique used for the integrated circuit (IC) industry, but the current strategies employed are blocked by optical diffraction. Thus, higher-resolution approaches such as X-Ray lithography and emerging lithography technologies have been explored to fabricate structures in the sub-100-nm range (see e.g., [1–6]).

Recently, electrochemistry at the nanoscale is strongly emerging because of significant advantages such as a low cost, simplicity, and compatibility with a wide range of micropatterning processes [7]. Especially, the ability to combine electrochemical techniques with several patterning approaches can be exploited for the micromachining [8, 9] and for shrinking the dimensions of structures below 100 nm (see, e.g., Ref. [10]). In this context, use of electrochemical approaches in conjunc-

T. Djenizian (✉)
Laboratoire MADIREL (UMR 6121), Université de Provence-CNRS, Centre Saint Jérôme, F-13397 Marseille Cedex 20, France
e-mail: thierry.djenizian@univ-provence.fr

P. Schmuki, S. Virtanen (eds.), *Electrochemistry at the Nanoscale,* Nanostructure Science and Technology, DOI 10.1007/978-0-387-73582-5_4,

tion with technologies based on charged particle beam lithography is also a convenient way for the nanostructuring of surfaces and the fabrication of ultra-small structures.

Charged particles beam lithography approaches include techniques using beam of electrons or ions, so-called electron-beam lithography (EBL) and focused ion beam lithography (FIBL), respectively. The process steps of these methods are similar to that described for photolithography, except that the transfer of the pattern is not achieved through the use of a mask but by scanning directly the focused particle beam across the surface [11, 12].

In this chapter, we report different strategies using the high-resolution potential of these direct writing approaches to achieve electrochemistry at the nanoscale.

2 Theoretical Aspects

2.1 Generality

Electron and ion beams are successfully used in a lot of different working areas. Although, especially electron beams are mainly used for microscopic imaging or material characterization by different techniques of electron microscopy, the number of applications increases where particle beams are used for material processing. Material processing includes not only structuring of sample surfaces by material removal or deposition, but also the application of energetic particle beams enables the well-defined and controlled modification of material properties in the surface near the regions of the specimen. For example, it is possible to alter the optical [13], mechanical, or electrical characteristics of solids by irradiation with energetic electrons or ions. In semiconductor technology the implantation of ions is used for doping of semiconductor crystals and is one of the fundamental processes for the fabrication of integrated circuits [14]. In the area of tribology, surface hardening by irradiation with energetic particles enables the fabrication of components showing increased wear resistance [15–17]. The alteration of the refractive index of materials due to irradiation with electrons or ions is also used for the fabrication of optoelectronic elements, for example, light guides [18].

All kinds of material processing by energetic particles do have in common that they are based on effects, which originate from the interaction of the energetic particles with the solid. This chapter briefly describes the theoretical background. For readers interested in a more detailed treatment literature quotations will be given.

2.2 Interaction of Energetic Particles with Solids

Energetic particles, that is, electrons or ions accelerated within an electric field, interact with atoms or molecules when penetrating a specimen. Due to these interactions, the particles are scattered and energy is transferred to the specimen. There are different inelastic and elastic effects, which can occur during the irradiation of

solids with charged particles. Collisions can take place between the incident particles and bound electrons or between the incident particles and nuclei or whole atoms of the stopping matter. During elastic interactions, the internal structure of the atoms and the energy of the atoms remain roughly unchanged. Inelastic collisions result in energy loss due to the excitation or ionization of atoms or molecules or due to nuclear excitation or nuclear reactions. Also, X-ray *bremsstrahlung* and *Cerenkov* radiation are effects, which reduce the total energy of the system. Which kind of the effects predominates depends upon the mass and the energy of the energetic particles and also upon the mass and the atomic number of the solid. In general, within the energy range normally used for material processing, with particle beams inelastic collisions with electrons and elastic nuclear collisions are the dominating effects. Low-probability inelastic nuclear collisions, and also elastic collisions with electrons, resulting only in low-angle scattering can be neglected.

2.3 Scattering of Particles

The probability of a particle undergoing any kind of interaction with an isolated atom is determined by the interaction cross-section. On the assumption that inelastic and elastic processes are independent of each other, a total scattering cross-section σ_{T} can be defined, which is the sum of the elastic $\sigma_{\mathrm{elastic}}$ and the inelastic scattering cross-section $\sigma_{\mathrm{inelastic}}$.

$$\sigma_{\mathrm{T}} = \sigma_{\mathrm{elastic}} + \sigma_{\mathrm{inelastic}} \tag{1}$$

The total cross-section Q_{T} for scattering of a particle from a specimen containing N atoms per unit volume can be defined as [19] and Q_{T} can be regarded as the number of scattering events per unit path that a particle travels through the sample.

$$Q_{\mathrm{T}} = N\sigma_{\mathrm{T}} \tag{2}$$

The energy transfer and kinematics in elastic collisions between two isolated particles can be solved by applying the principles of conservation of energy and momentum. Under the assumptions, usually made in the description of the scattering processes between energetic particles in solids [20]:

- binary collisions only are considered
- the loss of energy due to excitation or ionization of electrons does not influence collision dynamics
- one of the two interacting particles is initially at rest the energies of the scattered projectile and of the recoil atom can be calculated [21].

Figure 1 shows a typical scattering process between two particles with unequal masses M_1 and M_2. In the laboratory system, the incident particle (initial kinetic

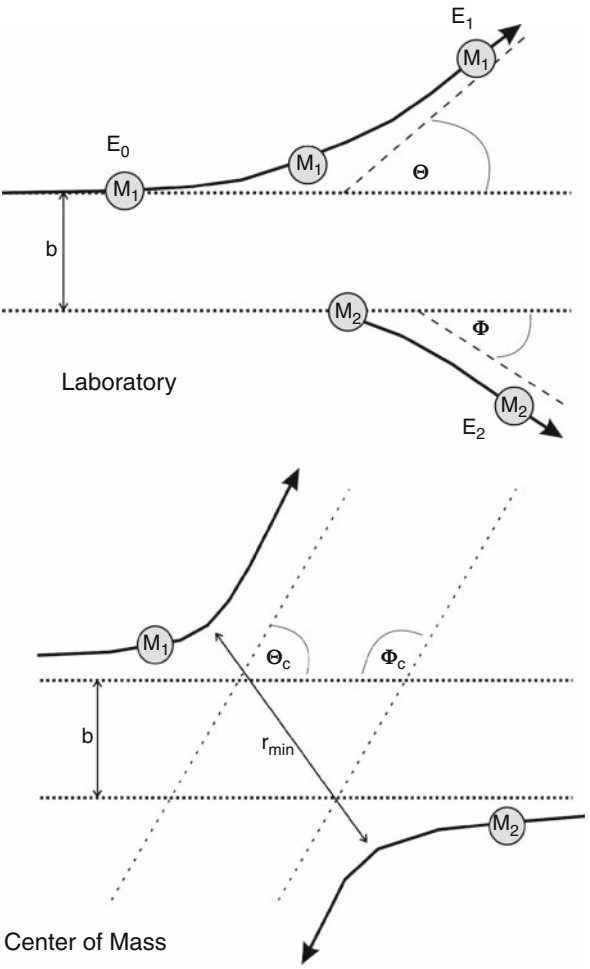

Fig. 1 Elastic collision diagram between particles of mass $M1$ and $M2$, scattering angle Θ and Φ, impact parameter b, in laboratory system and center-of-mass system

energy, E_0) is deflected by the angle Θ and transfers an energy E_2 to the recoiling atom, which leaves its original position at the angle Φ.

Energy of the scattered projectile (laboratory system) [22]:

$$K = \frac{E_1}{E_0} = \frac{\left[\mu \cos\Theta + \left(1 - \mu^2 \sin^2\Theta\right)^{1/2}\right]^2}{(1+\mu)^2} M_1 \leq M_2 \tag{3}$$

$$\frac{E_1}{E_0} = \frac{\left[\mu \cos\Theta \pm \left(1 - \mu^2 \sin^2\Theta\right)^{1/2}\right]^2}{(1+\mu)^2} M_1 > M_2 \tag{4}$$

Energy of the recoil nucleus (laboratory system):

$$\frac{E_2}{E_0} = 1 - \frac{E_1}{E_0} = \frac{4M_1M_2}{(M_1 + M_2)^2}\cos^2\Phi \tag{5}$$

E_0: energy of the incident particle
E_1: laboratory energy of the scattered particle
E_2: laboratory energy of the recoiling target
M_1, M_2: mass of incident projectile and target atom
μ: mass ratio M_1/M_2
Θ: laboratory angle of the scattered projectile
Φ: laboratory angle of the recoiling target atom

The angular distribution of projectiles scattered from an atom is described by the angular differential scattering cross-section. This quantity gives a measure of the probability of scattering an energetic particle through an angle between Θ and $\Theta + d\Theta$ into a solid angle $d\Omega$. The differential cross-section has units of area. The differential cross-section is normally calculated for center-of-mass coordinates. The energy E_2, transferred to the target atom and often referred to as T, is given by:

$$T \equiv E_2 = E_0\frac{2M_1M_2}{(M_1 + M_2)^2}(1 - \cos\Theta_C) \tag{6}$$

Conversion of scattering angles from the laboratory system to the center-of-mass system is given by:

$$\Phi = \frac{\pi - \Theta_C}{2} = \frac{\Phi_C}{2} \tag{7}$$

$$\tan\Theta = \frac{M_2\sin\Theta_C}{M_1 + M_2\cos\Theta_C} \tag{8}$$

Θ_C: center-of-mass angle of the scattered projectile
Φ_C: center-of-mass angle of the recoiling target atom

The scattering angle Θ_C is given by the classical scattering integral [22], which gives the angular trajectory information for a two-body central-force scattering:

$$\Theta_C = \pi - 2b\int_0^{u_{\max}} \frac{du}{\left[1 - \frac{V(u)}{E_C} - (bu)^2\right]^{1/2}} \tag{9}$$

$u = 1/r$
$r = r_1 + r_2$, is the distance between particles in the center-of-mass system
$V(u)$: interaction potential

E_C: total kinetic energy in the center-of-mass system
u_{max}: reciprocal value of the minimum distance between the particles $1/r_{min}$
B: impact parameter

When the interaction between colliding particles is purely Coulombic and projectile and target nucleus are treated as pure nuclei, this means the interaction potential $V(u)$ can be written as the Coulomb potential, the elastic scattering in the center-of-mass system can be described by the equation of Rutherford, which was derived for the scattering of α particles [23]:

$$\frac{d\sigma(\Theta_C)}{d\Omega} = \frac{e^4}{16}\frac{Z_1^2 Z_2^2}{E_C^2}\frac{1}{\sin^4\frac{\Theta_C}{2}} \tag{10}$$

$\frac{d\sigma(\Theta)}{d\Omega}$: angular differential scattering cross section
Z_1: atomic number of the scattered particle
Z_2: atomic number of the target atom
E_C: total kinetic energy in the center-of-mass system
$e^2 = \frac{e_0^2}{4\pi\varepsilon_0}$: e_0 electron charge

The equation of Rutherford is based on the assumption that two-point charges interact with each other by Coulomb forces, and no screening by the surrounding electrons takes place. It is assumed that the kinetic energy of the incident particles is sufficiently high to penetrate the electron cloud and to approach the nucleus, so that screening of the nucleus by the electron cloud can be neglected. Deviations from the equation can occur for high and low particle energies. For high energies, the distance between the incident particle and the nucleus becomes small and nuclear forces can influence scattering. At high energies, also relativistic effects can alter the scattering. Because of their low mass, the velocity of electrons with an energy of more than 100 keV is already high enough that relativistic effects have to be considered. Within the energy range normally used for material processing by ions, the velocity of the energetic ions is significantly lower and relativistic effects can be neglected. To give a more accurate description of the scattering of high-velocity electrons, a differential cross-section corrected for relativity can be used [24]:

$$\frac{d\sigma(\Theta_C)}{d\Omega} = \frac{e^4}{16}\frac{Z^2}{E_C^2}\frac{1}{\sin^4\frac{\Theta_C}{2}}\left(\frac{m_0c^2 + E_0}{2m_0c^2 + E_0}\right)^2 \tag{11}$$

E_0: kinetic energy of the electron and
m_0c^2: rest mass energy of the electron

If the particle energy is not sufficient to get close to the nucleus, the screening effect of the surrounding electron cloud, which acts to reduce the differential cross-section, cannot be neglected. For electrons and light ions, this screening effect can be described by the modified Rutherford differential cross-section: [25]

$$\frac{d\sigma(\Theta_C)}{d\Omega} = \frac{e^4}{16}\frac{Z_1^2 Z_2^2}{E_C^2}\frac{1}{\left[\sin^2\frac{\Theta_C}{2} + \left(\frac{\Theta_0}{2}\right)^2\right]^2} \tag{12}$$

Θ_0 is the so-called screening parameter for electron scattering given by: [26]

$$\Theta_0 = \frac{0.117 Z^{1/3}}{E_C^{1/2}} \tag{13}$$

E_C in keV

It can be described by a particular scattering angle. When the scattering angle is greater than Θ_0, electron–electron interactions can be neglected and the nuclear interaction is dominant.

For heavy particles of low velocity, and in the case of relatively distant collisions, the screening effect of the electrons cannot be neglected. In order to describe the scattering of particles, the interaction potential between two atoms has to be known exactly. The detailed calculation of the potential between two atoms is only possible by numerical calculations, taking into account the electron distribution within the shell of the interacting particles. In order to enable an analytical calculation of the interaction between atoms, the potential is described by a Coulomb potential, which additionally includes a suitable screening function, taking into consideration the screening of the nuclei.

$$V(r) = \frac{Z_1 Z_2 e^2}{r}\varphi\left(\frac{r}{a}\right) \tag{14}$$

$\varphi\left(\frac{r}{a}\right)$: screening function
a: screening parameter

In literature, many different screening functions used for the analytical solution of eq. (1) can be found [27–29]. Very good accordance with numerical data can be achieved by applying the so-called ZBL screening function derived by J.F. Ziegler, J.P. Biersack, and U. Littmark [30].

2.4 Stopping of Particles in Solids

When an energetic particle penetrates a solid, it undergoes a series of collisions with atoms and electrons in the specimen. Depending on energy and mass of the incident particle as well as on the target material, the incident particle loses energy at a rate dE/dx. The kinetic energy of the projectiles, not scattered backward and leaving the specimen as the so-called "reflected" particles, is totally transferred to the target and the particle comes to rest in the solid. As the amount of energy lost per collision and the distance between collisions are random processes, the path length of identical particles impinging the surface with identical energy differs and a distribution in

depth arises. The range R is determined by the energy loss along the path of the particle

$$R = \int_{E_0}^{0} \frac{1}{\mathrm{d}E/\mathrm{d}x} \mathrm{d}E \tag{15}$$

E_0 is the incident energy of the particle penetrating the specimen. The energy loss $\mathrm{d}E$ per traveled path $\mathrm{d}x$ is determined by the screened Coulomb interactions with atoms of the specimen and electrons. As already mentioned, two effects dominate the stopping of particles in solids: nuclear collisions, in which energy is transferred as kinetic energy to a target atom as a whole, and electronic collisions, in which the moving particle excites or ejects bound and free electrons. On the assumption that the two mechanisms of energy loss are independent of each other, as a good approximation, the energy-loss rate $\mathrm{d}E/\mathrm{d}x$ can be expressed as:

$$\frac{\mathrm{d}E}{\mathrm{d}x} = \left.\frac{\mathrm{d}E}{\mathrm{d}x}\right|_n + \left.\frac{\mathrm{d}E}{\mathrm{d}x}\right|_e \tag{16}$$

$\left.\frac{\mathrm{d}E}{\mathrm{d}x}\right|_n$ nuclear stopping
$\left.\frac{\mathrm{d}E}{\mathrm{d}x}\right|_e$ electronic stopping

Due to the transfer of energy to target atoms, nuclear collisions can result in large, discrete energy losses and also lead to significant scattering of the projectile. Predominately for heavy ions, this process is responsible for the displacement of atoms from their lattice sites, and therefore for the production of damage. Electronic collisions involve almost no scattering of the particle, negligible lattice disorder, and much smaller energy loss per collision. The relative importance of the two effects depends on the energy, mass, and atomic number of the particles and on mass, atomic number, and structure of the specimen. Typical units for the energy-loss rate are electron-volt per nanometer. Stopping cross-sections for nuclear and electronic stopping $S_{n/e}$, are defined as:

$$S_{n,e} = -\frac{1}{N}\left(\frac{dE}{dx}\right)_{n,e} \tag{17}$$

N: atomic density

At low energies, elastic collisions with the nuclei dominate. With increasing velocity v, the energy loss due to nuclear collisions decreases and the inelastic interaction with free and bound electrons becomes the main process of interaction. Within the low-energy region, under the assumption [31] that the electrons form a free-electron gas, it can be shown that the electronic stopping cross-section is proportional to the velocity of the ions, and therefore proportional to the root of

the energy. For higher energies, the electronic stopping cross-section goes through a maximum and then decreases proportionally to v^{-2} [22]. In this energy range, where the interaction potential for collisions is assumed purely Coulombic, the Bethe–Bloch theory [32, 33] is valid, which can also be applied for the stopping of electrons in solids. The electronic stopping cross-section is given by the Bethe formula

$$S_e = -\frac{1}{N}\left(\frac{dE}{dx}\right)_e = \frac{4\pi Z_1^2 e^4 Z_2}{m_e v^2}\left(\frac{M_1}{m_e}\right)\ln\frac{2m_e v^2}{I} \tag{18}$$

For most elements, the average excitation energy I can be approximated by:

$$I \cong 10Z_2 \tag{19}$$

Calculated and experimental data for the average excitation energy can be found in [34]. For high energies, the Bethe formula has to be corrected for the effect of relativity and the electronic stopping cross-section is given as:

$$S_e = -\frac{1}{N}\left(\frac{dE}{dx}\right)_e = \frac{4\pi Z_1^2 e^4 Z_2}{m_e v^2}\left(\frac{M_1}{m_e}\right)\left[\ln\frac{2m_e v^2}{I} - \ln\left(1-\beta^2\right) - \beta^2\right] \tag{20}$$

$\beta = v / c$

c: velocity of light

After transferring their kinetic energy totally to the target, the kinetic particles come to rest in the solid. Due to the collisions with the atoms of the specimen, the particles do not travel in a straight path. The net penetration into the material, that is, the projection of the range R on the incidence direction of the particle, is called the projected range.

As the interactions between particles and atoms are stochastic processes, the path length of identical particles impinging the surface with identical energy differs and a distribution in depth arises. The distribution in projected ranges is referred to as the range distribution. The most probable projected range is the so-called average or mean projected range R_p. The standard deviation of the range distribution is referred to as the projected range straggling σR_p.

Because of the high difference in mass between impinging electrons and the nuclei of the specimen, the energy loss of the electrons due to nuclear collisions can be neglected. Therefore, the deceleration of the electrons is only caused by the interaction with shell electrons. Referring to the Bethe formula, for electrons with energy between 10 keV and 100 keV the average range of the electrons can be calculated.

For ions with not too high kinetic energy, the loss of energy due to nuclear collisions cannot be neglected and in comparison to electrons, the penetration depth

is reduced. For amorphous solids, at low ion doses N_{imp} and, under the assumption that all ions will be implanted, the range distribution is roughly Gaussian and can be described as:

$$N(x) = \frac{N_{imp}}{\sqrt{2\check{s}}\Delta R_P} \exp(-\frac{(x - R_P)^2}{2\Delta R_P^2}) \tag{21}$$

with a maximum doping concentration

$$N_{\max} = \frac{N_{imp}}{\sqrt{2\check{s}}\Delta R_P} \tag{22}$$

The deceleration of energetic particles in a solid by inelastic collisions leads to the excitation of target atoms and to a whole range of signals used for imaging and analytical purposes. The most important signals are X-rays and secondary electrons. Characteristic X-rays are produced if an amount of energy higher than the excitation energy is transferred to a bound electron which, as a result, is ejected and replaced by an electron from an outer shell. This transition can be accompanied by the emission of X-rays or Auger electrons. Besides characteristic X-rays, *Bremsstrahlung* X-rays can be also detected. This radiation results from kinetic particles that inelastically interact with the nucleus. The deceleration of the particle by the Coulomb field of the nucleus leads to the emission of X-rays. Depending on the strength of interaction, the particle can suffer any amount of energy loss. For electrons, the probability for the generation of *bremsstrahlung* can be described as: [35]

$$N\,(E) = \frac{K\,Z(E_0 - E)}{E} \tag{23}$$

$N(E)$: number of *bremsstrahlung* photons with energy E
E_0: energy of the electrons
K: Kramer's constant
Z: atomic number of the atom

Secondary electrons are electrons of the target material ejected due to the interaction with the penetrating particle. Besides Auger electrons, which, as already mentioned, can be ejected from an inner shell when an ionized atom returns to the ground state, there are two additional types of secondary electrons, which can be distinguished by kinetic energy. Electrons in the conduction or valence bands can be easily ejected and have energies typically below 50 eV. The emission process of this so-called "slow" electrons, which are used to form images of the specimen surface, can be quite complex, and the different production processes cannot be described by one cross-section. The number of secondary electrons is highest at about 5 eV and is close to zero for energies $\geq$50 eV. In contrast, "fast" electrons are strongly bound electrons, which are ejected from inner shells and can have up to 50% of the beam energy when they are ejected.

2.5 Radiation Damage in Solids

During the stopping of energetic particles in solids, energy is transferred to the specimen in elastic and inelastic collisions. The energy transfer responsible for the generation of a number of useful signals, for example, secondary electrons used for imaging of the sample surface, unfortunately, also causes more or less significant rearrangement of the target structure. This so-called "radiation damage" not only affects the structure of the target but can also modify many other properties of matter, for example, density, elasticity, or electrical parameters. As far as electrical parameters are concerned, they especially affect the mobility, lifetime, and, under some circumstances, the carrier concentration [14].

The resulting damage depends mainly on the energy and mass of the projectile as well as on the mass of the target atoms. Inelastic collisions between impinging particles and electrons mainly result in interband transitions and ionization and give rise to chemical-bonding changes. Elastic collisions can result in the displacement of atoms from their lattice site. This effect, which is mainly due to ions and high-energy electrons, can produce collision cascades if the kinetic energy of the displaced atoms is sufficient to also displace other atoms. Collision cascades lead to an accumulation of the so-called Frenkel defects, a combination of a lattice vacancy and an interstitial atom, and also to complex lattice defects called clusters. With increasing particle dose, and thus growing density of beam-induced damage, the clusters overlap and a continuous damaged layer is formed. For a sufficiently high dose, the top layer of the specimen will be completely amorphized. It is assumed that at least 50% of the atoms have to be displaced for an amorphous layer to be formed. The extent of radiation damage created is determined by the kind and energy of the projectiles, the temperature of the specimen, the particle dose, and channeling effects, if the specimen possesses a crystalline structure. Channeling effect denotes the increased penetration of particles along major axes and planes within a monocrystalline target, because of the reduced nuclear stopping within channels formed by the symmetrical arrangement of the lattice atoms. In order to displace an atom from its lattice site, a minimum amount of energy, that is, displacement energy E_d, has to be transferred. If the transferred amount of energy is not sufficient to knock-out the atom of its atomic site, the struck atom undergoes large amplitude vibrations and no Frenkel pair will be created. The vibrational energy of the struck atom is quickly shared with nearest neighbors, and phonons will be generated. These collective oscillations of the crystal lattice result in heating of the sample and may cause damage. Specimen heating is difficult to measure experimentally because of the many variables that can effect the results, such as thermal conductivity, thickness, and surface condition of the specimen as well as the kinetic energy of the particles, and the current density of the particle beam. The effects of beam current and thermal conductivity on the specimen temperature for electrons were calculated by L.W. Hobbs [36].

Because of the crystallographic structure of a solid, the displacement energy for a lattice atom depends on the direction of the momentum of the target atom. Therefore, a range of displacement energies exists for the creation of a Frenkel pair. The average displacement energy is typically a factor one to two larger than the

Table 1 Minimum and average displacement threshold energies for some monoatomic materials [22]

Atomic number	Chemical symbol	Minimum displacement energy (eV)	Average displacement energy (eV)
6	Graphite	25	
6	Diamond	35	
12	Mg	10	
13	Al	16	27
14	Si	13	
22	Ti	19	
23	V	26	
24	Cr	28	
26	Fe (bcc)	17	
27	Co (hcp)	22	34
28	Ni	23	34
29	Cu	19	29
30	Zn	14	29
31	Ga	12	
32	Ge	15	
40	Zr	21	
41	Nb	28	
42	Mo	33	
46	Pd	26	41
47	Ag	25	39
48	Cd	19	36
49	In	15	
50	Sn (white)	22	
50	Sn (gray)	22	
71	Lu	17	
73	Ta	34	90
74	W	38	
75	Re	40	
78	Pt	33	44
79	Au	36	43
82	Pb	14	19
90	Th	35	44

minimum displacement energy. Table 1 gives the displacement energies for some monoatomic materials [22].

Based on the Kinchin–Pease formula [37], the number N_d of atoms displaced per incident particle can be calculated by:

$$N_d = \frac{E_n}{2E_d} \tag{24}$$

E_n is the total energy loss of a particle due to nuclear collisions and E_d is the displacement energy. Under the assumption that at least 50% of the atoms have to be displaced in order to create an amorphous layer, the critical dose for amorphization

can be calculated by:

$$D_a = \frac{E_d N}{\left(\mathrm{d}E/\mathrm{d}x\right)_n} \tag{25}$$

N: atomic density of the target material
$(dE / dx)_n$: energy deposited in nuclear collisions per unit distance

In real terms, the critical dose for amorphization is almost always higher than the value calculated by this equation, as effects, like the annealing arising during the bombardment of the specimen or collisions with already displaced atoms, are neglected [14].

2.6 Sputtering

The erosion of a specimen by energetic particle bombardment is called sputtering. In this process, incoming particles interact with atoms in the near-surface layer of the solid, and atoms at the surface are removed. This effect, which is especially pronounced in case of heavy ions and high doses, can be regarded as a kind of damage as it (e.g., during ion implantation) unintentionally modifies the topography of the sample and leads to an alteration of the implantation profile. However, sputtering is also a very desirable effect where material has to be removed intentionally, for example, for physical vapor deposition or in the field of micro- and nanostructuring, where focused ion beams are used for high-precision material removal. The most important parameter describing sputtering is the number of sputtered atoms per incident ion. This sputtering yield Y depends on energy and mass of the ions, the angle of incidence, and the structure and composition of the specimen. Based on a model of Sigmund [38] for vertical incidence and sufficiently high energy, the sputter yield is given by:

$$Y(E) = \frac{3}{4\delta^2 C_0}\frac{1}{U_0}\left(\frac{M_2}{M_1}\right)\cdot S_n(E) \tag{26}$$

C_0 is a constant ($C_0 = 0.5\pi\lambda_0 a^2$; $\lambda_0 = 24$; $a = 0.0219$ nm)
(M_2/M_1) is a numerically calculable function
U_0 is the surface-binding energy

For medium mass-ion species and not too high energies, the values of Y lie between 1 and 10. Values for Y for different projectile–target combinations can be found in [39].

Sputtering removes material from the surface of the specimen. The thickness d of the removed layer is given by:

$$d = Y\frac{N_{imp}}{N} \tag{27}$$

N: atomic density of the target material
N_{imp}: ion dose

The erosion of the sample surface modifies the implantation profile. Under some simplifying assumptions, the modification of the depth profiles can be calculated by [14]:

$$N(x) = \frac{N}{2Y}\left(\text{erf}\,\frac{x - R_P + N_{imp}\frac{Y}{N}}{\sqrt{2}\Delta R_P} - \text{erf}\,\frac{x - R_P}{\sqrt{2}\Delta R_P}\right) \tag{28}$$

For high-ion dose, an equilibrium condition is obtained with a maximum of concentration N_{max} at the surface:

$$N_{max} = \frac{N}{2Y}\text{erfc}\left(\frac{-R_P}{\sqrt{2}\Delta R_P}\right) \approx \frac{N}{Y}\text{for } R_P \geq 3\Delta R_P \tag{29}$$

3 Micro- and Nanostructuring by Electron-Beam Approaches and Electrochemical Reactions

Electrochemical technology has been combined with several electron-beam (e-beam) approaches to generate materials with features size that range from nanometers to micrometers in size. This section reports how to exploit electrochemistry with conventional EBL as well as alternative e-beam approaches to achieve the micro-and nanostructuring of the surfaces.

3.1 Microstructuring by Conventional EBL and Electrochemical Reactions

3.1.1 Basics on Electron-Beam Lithography

Electron-beam lithography (EBL) followed soon after the development of the scanning electron microscope (SEM) in 1955 [40] (see a description of a SEM in Fig. 2) and was one of the earliest processes used for IC fabrication dating back to 1957 [41]. The principle of pattern transfer based on EBL is depicted in Fig. 3. The lithographic sequence begins with coating substrates with a positive or negative resist. Then, direct e-beam exposure of the resist is achieved as it is depicted in Fig. 3a. In general, the e-beam-writing system is equipped with a lithographic tool in order to control accurately the displacement of the beam. Positive resists such as poly(methyl-methacrylate) (PMMA) become more soluble in a developing solvent after exposure, because weak radiation causes local-bond breakages and thus chain scission. As a result, the exposed regions containing material of lower mean

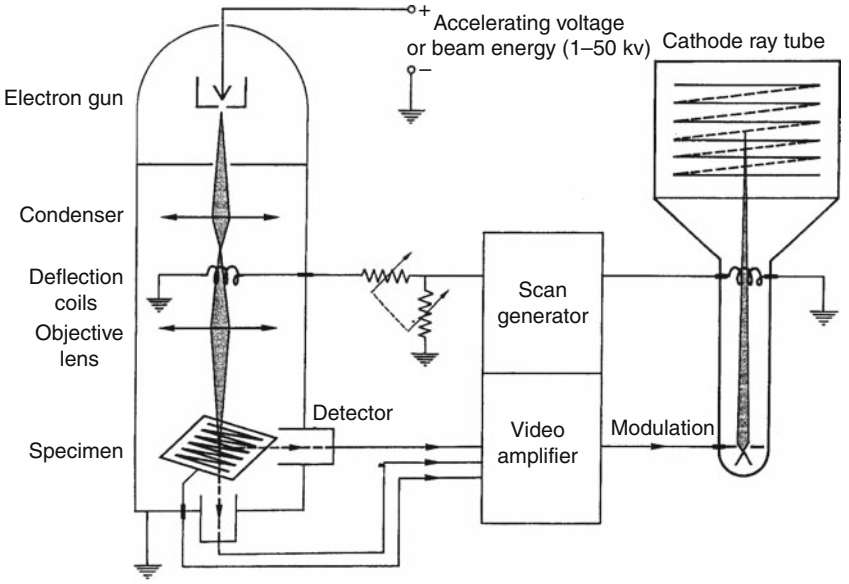

Fig. 2 Schematic drawing of a scanning electron microscope

molecular weight are dissolved after development (Fig. 3b). By contrast, negative resists become less soluble in solvent after exposure, because cross-linking of polymer chains occurs. In this case, if a region of a negative resist-covered film is exposed, only the exposed region will be covered by resist after development. Subsequently, the resist-free parts of the substrate can be selectively coated with metal – as it is shown in Fig. 3c – or etched before removal of the unexposed resist, leaving the desired patterns at the surface (Fig. 3d).

As early as 1965, sub-100-nm resolution was reported [42] and was optimized with improved electron optics and with the use of different strategies, such as membrane substrate, reactive ion etching, and lift-off process [43–52]. Compared with photolithography, a higher lateral resolution is achieved because the beam of electrons can be focused to produce probe size as small as 1 nm and electrons do not suffer from optical thin-film interference. However, several parameters other than the size of the beam determine the ultimate resolution of the process. Particularly, extent of the exposed volume in a layer of resist depends strongly on the scattering events because electrons are scattering not only within the resist but also within the substrate beneath the resist layer (see Fig. 4a). These scattered electrons slightly expose the resist in a halo around each of the exposed features. A dense array of features may contain enough scattered electrons to seriously overexpose the resist. The main characteristics of this so-called proximity effect, the range of backscattered exposure, and its relative intensity have been studied experimentally [53, 54] and by Monte Carlo calculations [55]. Chang proposed a two-Gaussian model to describe resist exposure from a point source [56]. A higher-intensity Gaussian width

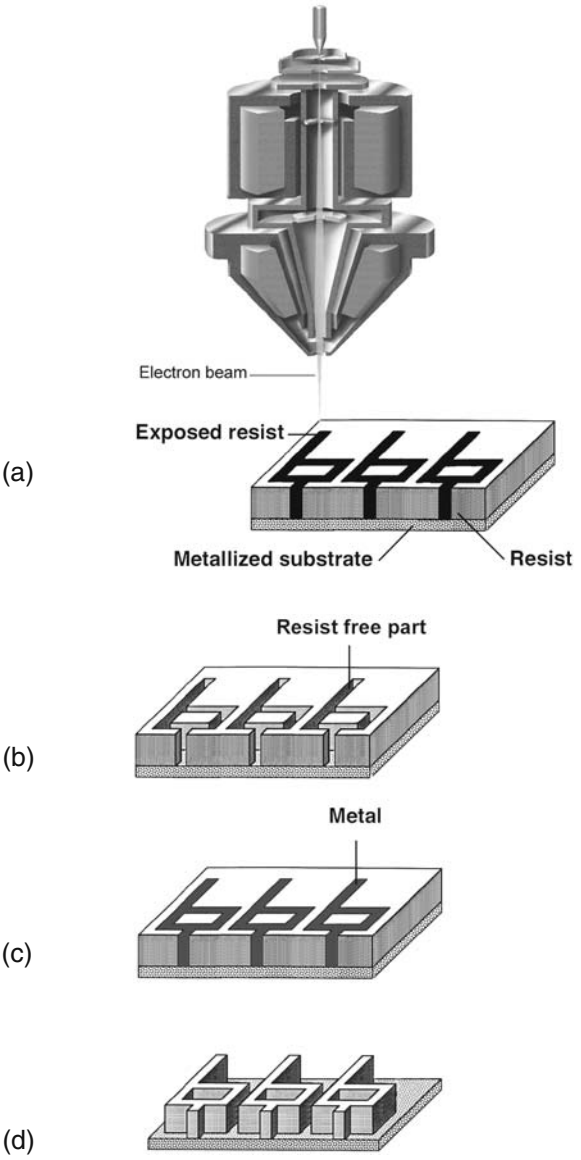

Fig. 3 Principle of the nanostructuring of surfaces using EBL technique and electroplating. E-beam exposure of a positive resist (**a**), removal of the exposed resist (**b**), filling of the resist-free locations with metal using electroplating technique (**c**), and removal of the unexposed resist leaving high-aspect-ratio metallic nanostructures at the surface (**d**)

describes the incident broadening in the resist and a less-intense broader Gaussian describes the distribution of the resist exposure due to the backscattered electrons (see Fig. 4b). The narrower distribution describes resolution and minimum feature size, while the backscattered electrons cause proximity effects. At present, these undesired effects have been minimized by using very high- and low-accelerating voltage or by correction methods. The resolution of EBL depends also on the

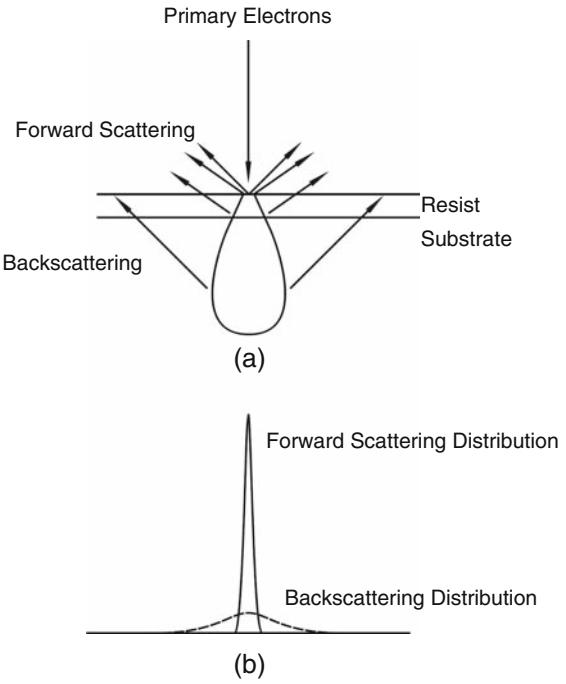

Fig. 4 Electron scattering events during exposure (**a**) and the corresponding exposure distributions (**b**)

chemical nature of the resist. PMMA was the first e-beam resist reported [57] and inspired the development of a various high-energy radiation resists. It is still commonly used because of its high resolution, but its low sensitivity and poor etch resistance under plasma conditions have forced the development of higher speed and resolution resists [58, 59]. Recently, new classes of resists, including organic self-assembled monolayers (SAMs), chemically amplified resists, and inorganic resists, have been developed to fabricate structures below 100 nm [60–65]. Thus, the electron scattering as well as the thickness and the nature of the resist determine the ultimate resolution (see, e.g., Ref. [66] for more details). Except for more recent reports of atomic resolution with a proximal probe (see, e.g., [67]), the resolution of EBL has been unsurpassed by any other form of lithography. However, the technique is far too slow for a large production and up to now is mainly used to produce masks, rapid prototyping of ICs, and specific small-volume production [63, 68].

3.1.2 Nanostructuring by EBL and Electroplating

Fabrication of metallic nanostructures has been widely explored using conventional EBL and lift-off techniques. However, this top-down approach cannot be used for the fabrication of high-aspect-ratio vertical structures, since gradual accumulation of materials at the top of the resist blocks and closes the opening of the structures during the evaporation of metal. Electroplating of metals into the holes formed

in PMMA resist is a convenient alternative to circumvent this problem [48]. For example, the fabrication of dense, ultrasmall magnetic arrays by filling nanoholes with electroplated Ni has been reported [69]. Electrodeposition of Ni was performed from Ni sulfonate electrolyte by potentiostatic experiments. Depending on the electroplating time, high-aspect-ratio Ni pillars or mushroom-like structures were obtained. Figure 5 shows a SEM micrograph of mushroom-shaped micromagnetic arrays grown by overplating after removal of PMMA by oxygen plasma etching. This bottom-up approach has been also used to produce arrays of 30-nm magnets with 80-nm pitch (distance between two magnets). From the viewpoint of a practical use, this packing density translates into an equivalent memory storage capacity of over Gbit/in^2. The density of the magnetic arrays can be further increased by optimizing the EBL parameters. Under optimal conditions, the formation of 12-nm holes in 100-nm thick PMMA resist with spacing of 45 nm have been reported showing the high resolution achieved by EBL and electrodeposition of metals [69]. Combining EBL and electrochemical deposition has been also used to fabricate CdSe pillars, with diameters in the range from 180 nm to 1 μm and a fixed height of 400 nm. Depending on the size of such structures, enhanced photoluminescence (PL) has been reported, thus opening potential application for cavity resonance in the submicrometer scale [70]. The use of this template strategy has been also exploited for the fabrication of nanometer-sized metallic wires, superconducting nanowires, and magnetic multilayers [71].

3.1.3 Nanostructuring by EBL and Electrochemical Etching

A similar approach has been investigated for the formation of monocrystalline pore arrays in anodic alumina [72]. For this, a hexagonal patterns was written on the PMMA resist hole by hole with EBL. After removal of the irradiated parts, the pattern was transferred to the Al substrate by using a wet-chemical etch in phos-

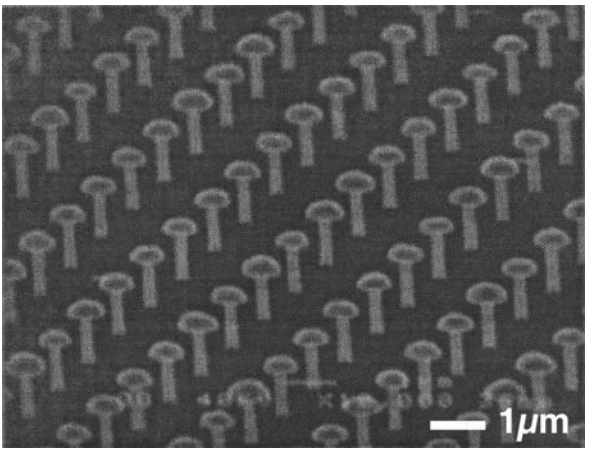

Fig. 5 SEM micrograph of an overplated micromagnet array showing the mushroom-shaped characteristic of isotropic metal deposition

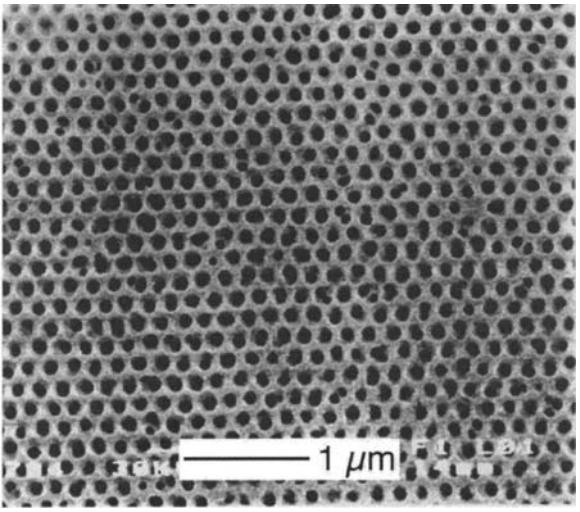

Fig. 6 Monocrystalline-pore arrays in ordered porous alumina prepared with prepattern-guided anodization. The prepattern with a pitch of 200 nm was induced by using EBL. (Reproduced by permission of the Electrochemical society, Inc.)

phoric and nitric acids. Then, PMMA was removed and the Al substrate was finally anodized in an oxalic acid solution under constant voltage. When the pore distance, which depends on the anodic voltage, matches the prepattern pitches well, the pattern can act as initiation point and guide the pore growth in the anodic film. Figure 6 shows a SEM micrograph of an ordered-pore array prepared with a 200-nm interpore distance. In this case, the anodic voltage was adjusted to 85 V based on the relationship between the pore distance and the anodic voltage. Under these conditions, very high aspect ratios (around 500) could be achieved. EBL has been also utilized for the direct microstructuring of porous silicon without the use of any sensitive resists [73]. It has been reported that the direct e-beam irradiation of electrochemically etched silicon can locally passivate the surface. This e-beam-induced enhancement of reactivity can subsequently be exploited for the selective dissolution of the exposed areas (see Fig. 7a). The ability to selectively etch silicon has been also investigated by cross-linked PMMA on porous silicon [74]. Although PMMA is usually known as a positive resist, the use of electron doses higher than 12 mC/cm^2 causes cross-links leading to a negative-tone resist behavior. Thus, this feature can be exploited to perform selective electrochemical processes (anodization) and fabricate microtips and nanomolds as shown in Fig. 7b.

3.2 Electrochemical Micropatterning Using E-beam Modification of SAMs

3.2.1 Self-Assembled Monolayers (SAMs)

SAMs are composed of organic molecules which consist of three building blocks: a head group that binds strongly to a substrate, a tail group that constitutes the

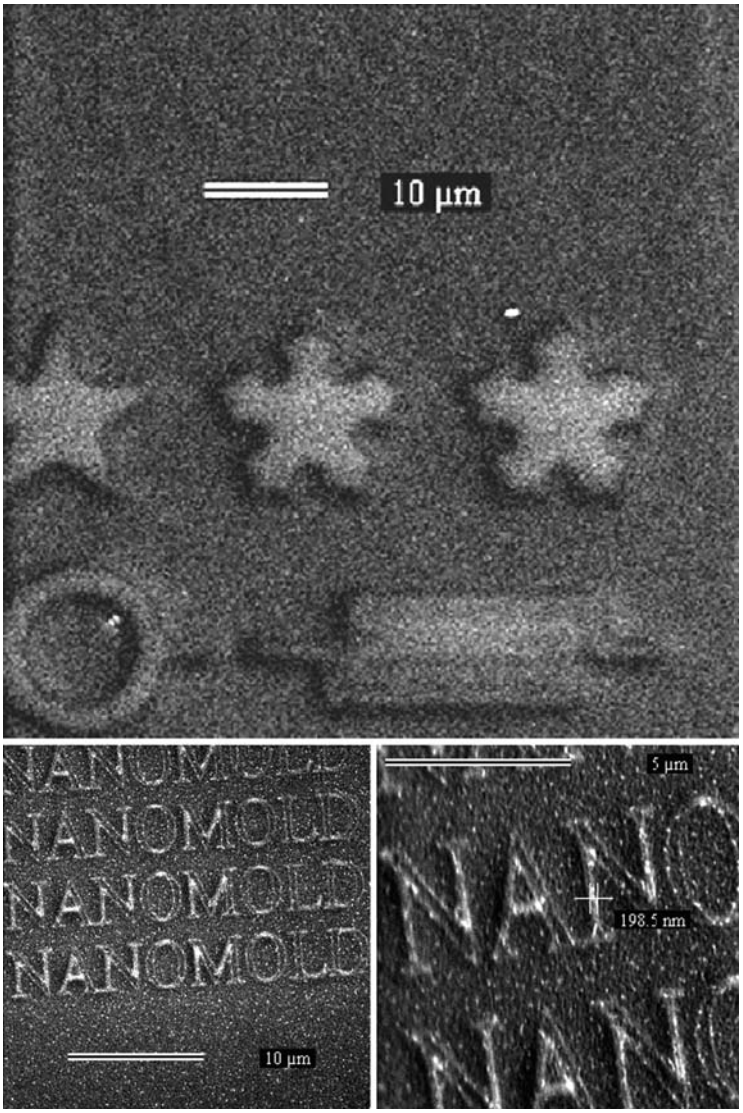

Fig. 7 SEM images of micropatterned porous silicon surfaces obtained by selective dissolution of e-beam irradiated areas (**a**) and by electrochemical etching through cross-linked PMMA mask (**b**)

outer surface of the film, and a spacer that connects head and tail. These molecules can be covalently anchored to different surfaces, such as metals, semiconductors, and oxides, with a typical thickness of 1–2 nm and an intermolecular spacing of 1–0.5 nm [75]. The interest in the general area of self-assembly, and specifically in SAMs, is mainly driven by their remarkable physical and chemical properties. In contrast to ultrathin films formed by conventional techniques, such as molecular-

beam epitaxy (MBE) and chemical vapor deposition (CVD), SAMs are much more dense, homogeneous, extremely thin, highly ordered, oriented, and stable even when they are subjected to a harsh environment. For a larger overview on SAMs, see, for example, Ref. [76].

With the development of microelectronic, chemical modification of semiconductor materials, and especially Si, has been extensively studied (see, for instance, Refs. [77, 78]). Functionalization of Si using SAMs consists of replacing silicon–hydrogen (Si–H_x) bonds by more robust silicon–carbon (Si–C) bonds [79]. The formation of this covalent bonding can be achieved, for example, by reaction of unsaturated, simple, and functional alkenes, with the Si surface using several procedures, including thermal activation [80] or UV light illumination [78]. Organic monolayers covalently attached to silicon surfaces display various advantages compared to SAMs of alkanethiols on gold surface and to octadecyltrichlorisilane (OTS) monolayers on SiO_2: high resistance of the monolayer in different organic and aqueous solutions (Si–C bond is very stable), good chemical passivation of the surface, existence of a wide range of chemical functionalities compatible with the Si–H bonds terminating the silicon surface. Furthermore, the functionalization methods are easy to carry out and highly reproducible. SAMs have many potential applications for the semiconductor technology, including surface passivation, electrochemical interfaces, microsensors, etc. (see, e.g., Refs. [81–83]). In addition, highly defined functionalization of surfaces with specific interactions can be produced with fine chemical control that make SAMs ideal candidates for biochemical and biomedical applications such as biosensing [84].

Recently, patterning of SAMs has been widely investigated because the possibility to achieve selective immobilization of biological molecules on solid substrate and then to manufacture microstructures carrying specific recognition have multiple issues in diagnostics, artificial biomolecular networks, and biologically integrated systems (lab-on-a-chip). In this context, many techniques have been employed to fabricate laterally patterned SAMs, including conventional photolithography [85], microcontact printing [6], scanning probe lithography [86], ion- beam lithography [87]. Furthermore, it has been reported that many SAMs are highly e-beam sensitive [61, 88] and can be ideal candidates for the development of a new class of positive- and negative-tone e-beam resists in a wet-chemical process [60]. As SAMs are extremely thin and composed of very small subunits, the forward beam scattering in the resist is eliminated, and the electrons inelastically generated in the substrate can leave the layer before undergoing substantial lateral travel. Compared with the use of high-molecular-weight resists, such as PMMA, a significant improvement of the lateral resolution can be achieved with SAMs.

3.2.2 Selective Electrodeposition Using E-beam-induced Modification of SAMs

The selective electrochemical deposition of metals can be achieved by the e-beam writing of surfaces covered with organic SAMs (see, e.g., [89]). Figure 8 shows

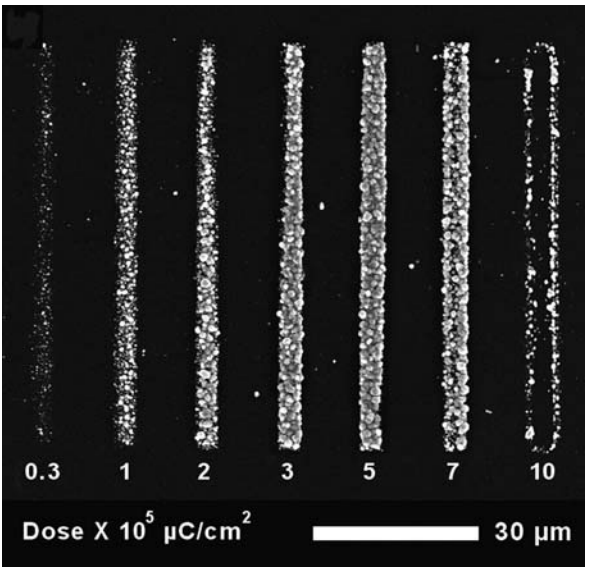

Fig. 8 SEM image of an e-beam-patterned silicon surface covered with an organic layer (1-decene) after electroplating of Cu

a SEM image of a silicon surface covered with an organic layer (1-decene) with four e-beam-modified patterns onto which copper has been electrodeposited. It has been reported that the selective copper deposition depends strongly on the electrochemical conditions as well as the electron dose. For relatively low electron doses, SAMs act as a positive-tone resist enhancing copper electrodeposition, whereas for relatively high electron doses, SAMs act a negative resist completely blocking the electrochemical process. According to surface-analysis experiments, this effect can be explained by the fact that partial removal of carbon chains occurs with low-electron doses, whereas at sufficiently high electron doses cross-linking of the molecules becomes predominant. Thus, e-beam-modified organic monolayers on Si surfaces combined with electrochemical processes is a viable alternative to achieve the fabrication of structures with features in the micrometer range.

3.3 Micro- and Nanostructuring by EBICD and Electrochemical Reactions

3.3.1 E-beam-Induced Deposition (EBID) Technique

EBID is a single-step and direct-writing technique using the beam of electrons to grow three-dimensional nanostructures. Due to the combination of high-resolution and 3D structure formation, EBID is highly appreciated in the field of exploratory nanodevice fabrication and has recently moved toward various applications for

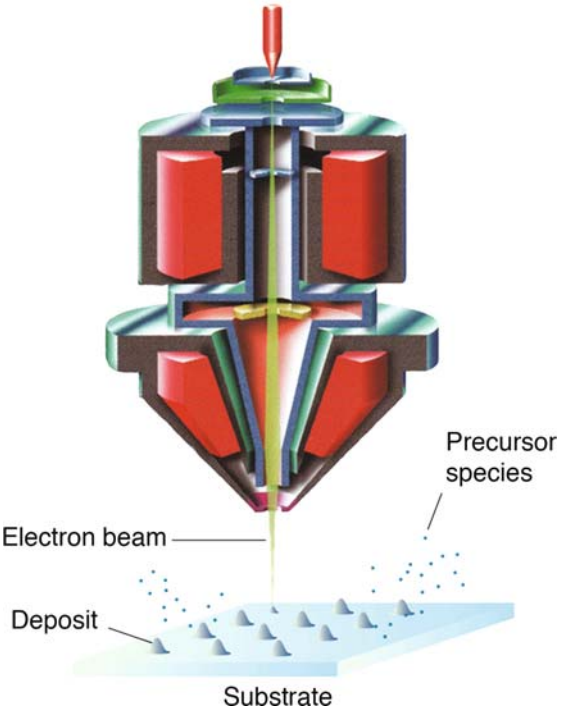

Fig. 9 Principle of EBID. The beam of electron cracks the precursor species introduced in the chamber of the SEM leading to the formation of a deposit at the point of impact of the beam

production of nanowires [90, 91], X-ray mask repair [92], photonic crystals [93], and a wide range of devices [94–98].

The principle of EBID is based on the fact that the beam of electrons decomposes adsorbed precursor molecules present in the chamber of the e-beam instrument resulting in a deposit at the point of impact of the beam as depicted in Fig. 9. The chemical composition of such deposits depends strongly on the nature of the precursor molecules introduced into the chamber of the e-beam instrument. When organometallic precursor species are injected, the e-beam-deposited materials show nanocomposite structures with metal nanocrystals of variable size embedded in an amorphous carbonaceous matrix [50, 99–102]. The resolution of the technique as well as the growth rate of such nanomaterials that is described by several models [103–107] are dependent on the vapor pressure in the chamber, the e-beam parameters, the exposure time, and the nature of the substrate (see, e.g., [92, 108–110]).

3.3.2 EBICD Technique

When decomposed precursor species are simply the residual hydrocarbon molecules issued from the pump oil, contamination writing, which consists of amorphous carbonaceous deposit is grown at the e-beam-treated locations [111–115].

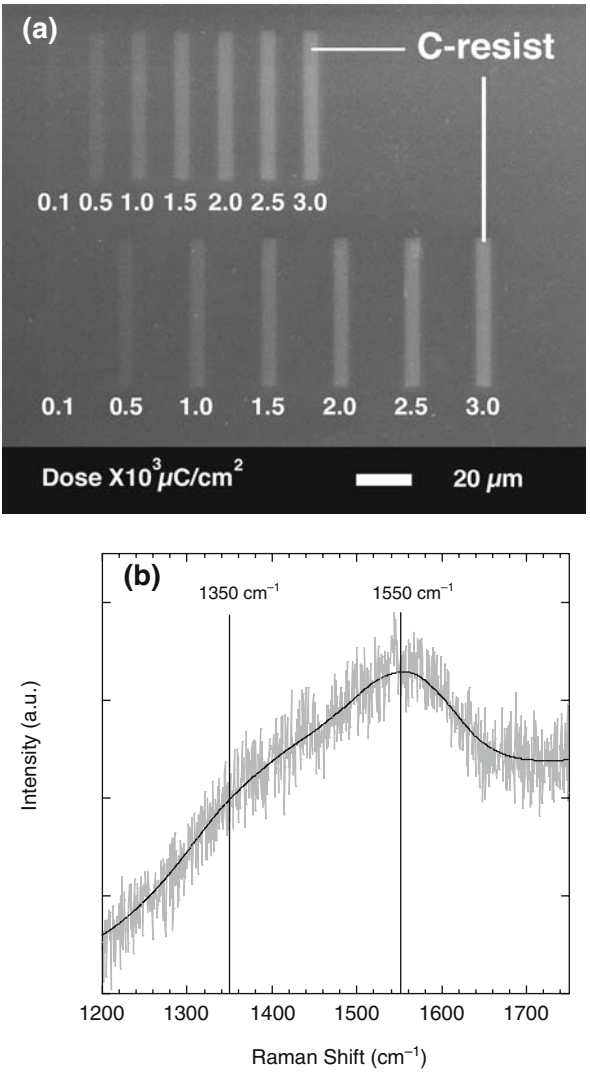

Fig. 10 SEM image of two series of seven C-patterns deposited with an increasing electron dose from the left to the right (**a**). Reprinted from Surface Science, T. Djenizian, L. Santinacci, H. Hildebrand, and P. Schmuki, vol. 524, "Electron beam induced carbon deposition used as a negative resist for selective porous silicon formation" p. 40, 2003, with permission from Elsevier. Raman spectrum obtained from a carbonaceous (**b**). (Reproduced by permission of the Electrochemical society, Inc.)

Figure 10 a shows a SEM image of ultrathin rectangular C-patterns, which have been deposited on a silicon surface using different electron doses. Figure 10b shows the Raman spectrum obtained from such C-deposited matter. In the region between 1200 cm^{-1} and 1800 cm^{-1} a broad peak centered around 1550 cm^{-1} (G-band) and the presence of the shoulder at around 1350 cm^{-1} (D-band) typical for amorphous carbonaceous films are observed [116, 117]. Examination of this spectrum confirmed that the sp^3- and sp^2-bonded carbon is incorporated in the e-beam-deposited material.

3.3.3 Contamination Lithography

As early as 1964, the fabrication of 50-nm lines ion milled into metal films using contamination resist has been reported [118]. Contamination lithography followed by ion milling of the pattern into the underlying metal has been developed [45] and exploited to produce the first functioning Aharonov–Bohm device [119]. Later, the use of carbonaceous mask has also been demonstrated for the selective growth of II–VI semiconductors by metalorganic-beam epitaxy [120]. Recently, it has been reported that e-beam-induced carbonaceous deposit can be used as a mask for electrochemical reactions, that is, it has been demonstrated that carbonaceous deposit in the nanometer-range thickness can block completely and selectively a wide range of electrochemical reactions [121]. According to the literature and surface-analysis measurements described above, e-beam-induced carbonaceous deposit is amorphous and consists mainly of a high amount of sp^3-bonded carbon [122–124] leading to chemical and physical properties very close to that observed for the diamond. Therefore, the negative-resist effect can be explained by the fact that this so-called diamond-like carbon (DLC) material is chemically inert and behaves as an excellent insulator hampering completely subsequent electrochemical reactions.

3.3.4 Micro- and Nanostructuring by EBICD Technique and Electrodeposition

Carbonaceous Masking of Electroplated Metals

Recently, it has been reported that e-beam-induced carbonaceous materials in the nanometer-range thickness can be used to block the electroplating of Au on semiconductor surfaces [125], as schematically depicted in Fig. 11. The high degree of selectivity that can be achieved by this technique is also confirmed for the selective electrodeposition of Cu.

Figure 12 shows a SEM image of n-type Si sample carrying a carbonaceous micropattern “LKO” after a cathodic potentiodynamic experiment. Clearly, the dark carbonaceous LKO micropattern surrounded by Cu crystallites corresponds to the masked area. Within this pattern, absolutely no deposited Cu particles could be detected even for very high-cathodic potentials. This result suggests the ability to exploit EBICD for the nanomasking of a wide range of electroplated metals on semiconductor surfaces.

Resolution of the Process

The fabrication of metallic nanostructures depends on the resolution achieved at the edge of the C-lines, which is governed by the morphology, size, and number of electrodeposited crystallites. Therefore, the control of electrochemical factors is a crucial step for optimizing the lateral resolution of the process. In the case of electroplating of metals onto semiconductor surfaces, the study of transients indicates that nucleation of 3D hemispherical clusters followed by diffusion-limited growth

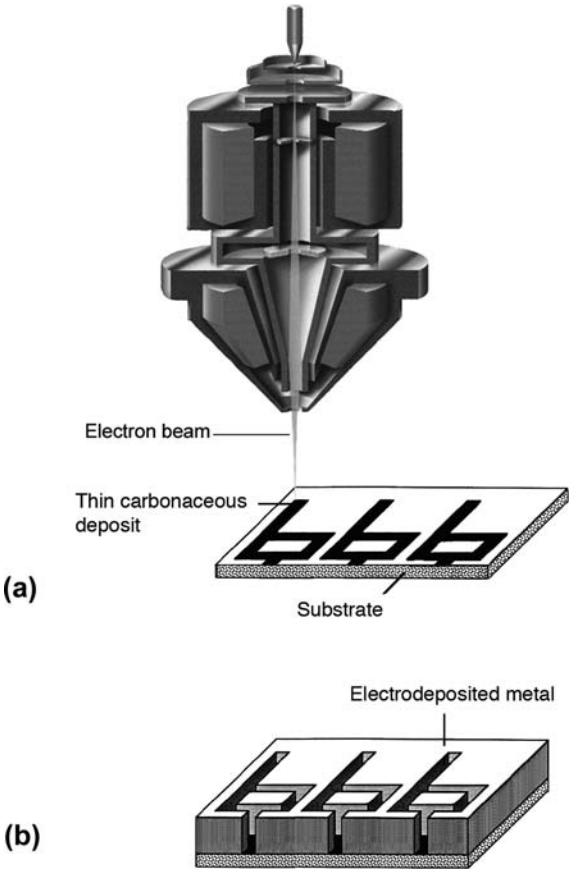

Fig. 11 Principle of the nanostructuring of surfaces using EBICD technique and electroplating. Ultrathin carbonaceous matter is deposited by direct e-beam exposure of the surface (**a**). Selective electrodeposition of metal at nonirradiated locations (**b**)

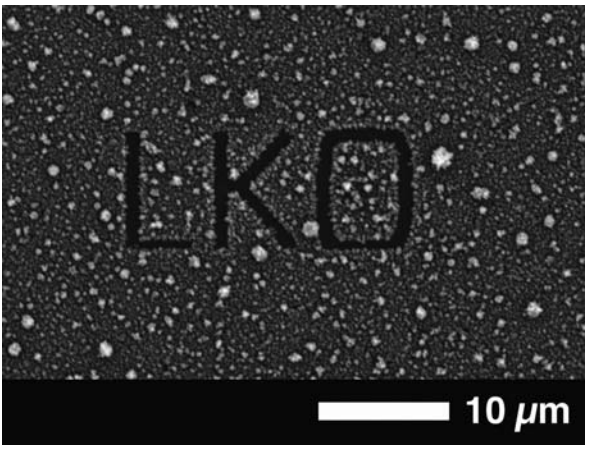

Fig. 12 Nanomasking effect of e-beam-induced carbonaceous deposits for electroplating of Cu. SEM image of n-type Si sample carrying a carbonaceous pattern "LKO" after electrochemical deposition of Cu performed by cathodic potentiodynamic experiment

occurs [126–128]. The 3D-island-growth mechanism or Volmer–Weber mechanism has already been observed for several systems and can be attributed to the relatively weak interaction energy between semiconductors and metals [129–134]. It has been observed that the density of nuclei as well as the size of the globular features size depend strongly on the applied potential, that is, the higher cathodic applied potential, the larger number of small crystallites. At relatively low cathodic potential, only few big crystallites are deposited onto Si. Using higher cathodic potential results in deposits entirely covering the Si surface with smaller mean size of particles. As the lateral resolution of the process at the edge of the C-deposit depends strongly on the formation of a smooth and continuous film, the creation of a large number of small crystallites is required because the coalescence of islands in an earlier growth stage leads to homogeneous layers. Therefore, deposits are preferentially formed at high cathodic potential.

Under optimized electrochemical conditions, it has been also shown that the resolution depends on the electron dose and the e-beam energy used for depositing the C-mask. Carbonaceous patterns written with a relatively high-beam energy (20 keV) revealed the presence of a C-background in the immediate vicinity of the predefined patterns. It is assumed that the large disk from which backscattered electrons re-emerge from the sample have enough energy to decompose organic molecules adsorbed at the Si surface. Such C-fog surrounding the patterns can block partially electrodeposition of metals and, consequently, a bad resolution is achieved at the edges of the C-lines. This effect is clearly apparent in Fig. 13a and b that show two Si samples carrying arrays of ten C-lines, equidistantly spaced (1.5 μm) and deposited using a low- and high-beam energy with increasing electron doses: $n{\cdot}\mathrm{C/cm^2}$ with $0.1 \leq n \leq 1$ after electrodeposition of Au [135].

Deposition of C-lines performed with a low-beam energy (5 keV) shows that independently of the electron dose, Au deposit between the C-lines is homogeneous and smooth leading to an excellent lateral resolution (Fig. 13a), whereas using a high-beam energy (20 keV) leads to coarse Au deposit between the C-patterns when the electron dose increases (Fig. 13b). Therefore, decreasing the spatial distribution of the backscattered electrons by decreasing the beam energy is a key step to improve the resolution of the process. In this case, Au nanowires and Au clusters in the sub-50-nm range were successfully fabricated under optimized electrochemical conditions as shown in Fig. 14a and b [135]. The linewidth of the nanowires as well as the size of the dots decrease by decreasing accurately the spacing between the carbonaceous lines. These results show clearly that combine contamination writing with electroplating of metals is a viable way to achieve the fabrication of metallic nanostructures on semiconductor surfaces in the sub-100-nm range.

3.3.5 Microstructuring by EBICD Technique and Electrochemical Etching

The masking effect of e-beam-deposited DLC has also been demonstrated for the electrochemical etching of materials in extremely aggressive environment. Particularly, carbonaceous masking has been investigated to block the porosification of Si

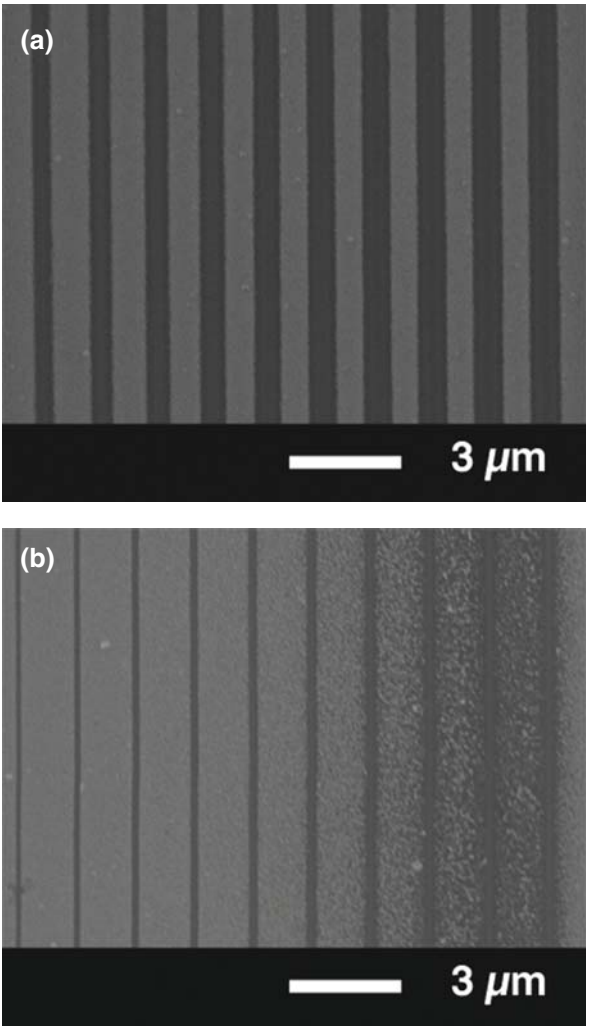

Fig. 13 Influence of the beam energy on the lateral resolution of the process. SEM images of Au electroplated on Si samples carrying arrays of ten C-lines produced with a relatively low 5 kV (**a**) and high 20 kV (**b**) accelerating voltage. (Reproduced by permission of the Electrochemical society, Inc.)

performed by galvanostatic experiments [136]. Figure 15a shows an optical image of a C-patterned p-Si sample after anodization in an HF-containing electrolyte. It is clearly apparent that the surface is modified, except at the locations carrying the C-patterns if a sufficient electron dose is used. Indeed, C-patterns deposited using electron doses higher than 1.0×10^3 μC/cm^2 do not suffer from etching. The unexposed area (surrounding the patterns) exhibits interference colors ranging from red to brown, which are typical of thin porous silicon layers. Within the rectangles the surface is intact; this region does not show signs of etching. Therefore, C-deposits produced with a dose higher than 1.0×10^3 μC/cm^2 can act as a mask for the electrochemical etching in HF solution, and thus constitute a negative resist blocking

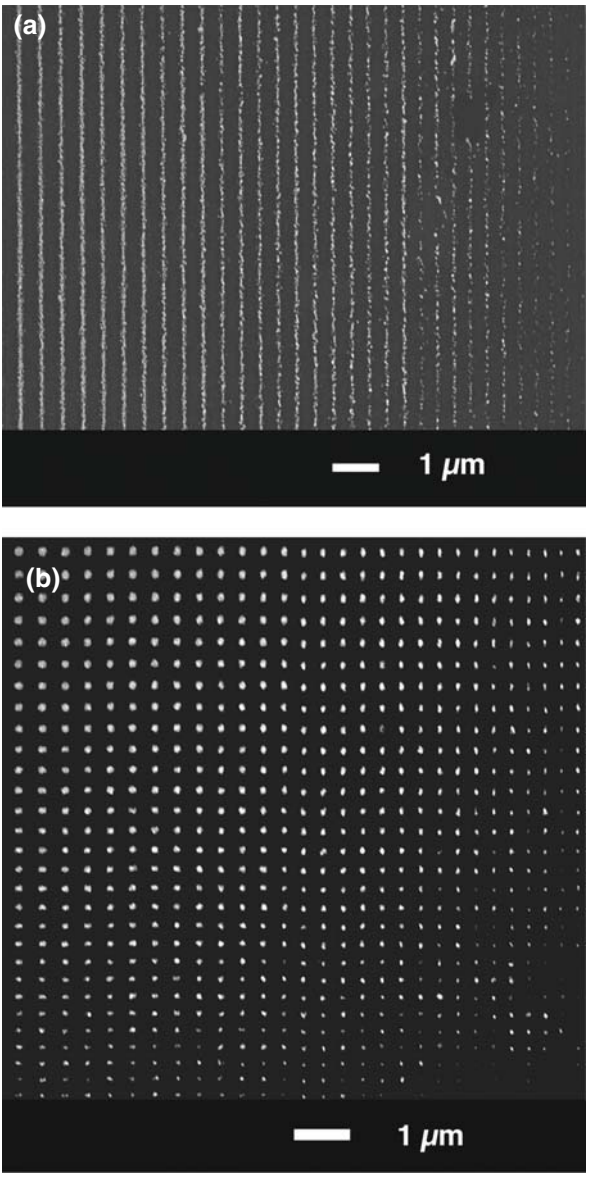

Fig. 14 SEM micrographs of Au nanowires (**a**) and Au clusters showing sizes in the sub-50-nm range (**b**). (Reproduced by permission of the Electrochemical society, Inc.)

completely and selectively the pore formation. Furthermore, selectivity in terms of optical properties of such micropatterned silicon surface has been corroborated by PL measurements. It has been reported that the PL intensity of locations protected by the C-mask deposited for electron doses higher than 1.0×10^3 μC/cm^2 is zero, and, thus, no light emitting structure is present within the C-patterned areas.

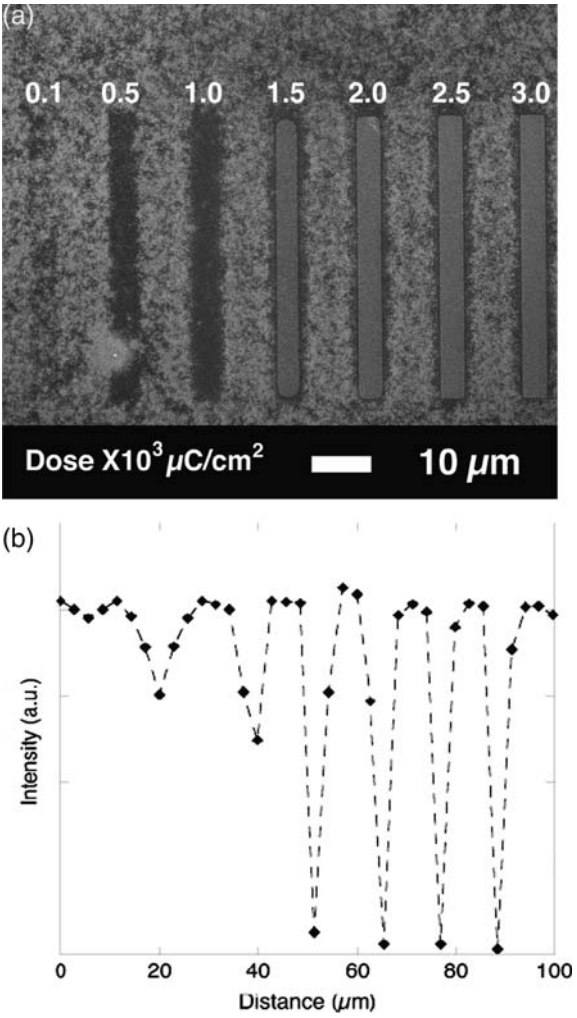

Fig. 15 SEM image of an etched Si surface carrying seven C-patterns (**a**). Luminescence scan performed across the C-patterns (**b**). Reprinted from Surface Science, T. Djenizian, L. Santinacci, H. Hildebrand, and P. Schmuki, vol. 524, "Electron beam induced carbon deposition used as a negative resist for selective porous silicon formation" p. 40, 2003, with permission from Elsevier

In contrast, the intensity between these C-deposits reveals a high value corresponding to the maximum PL response (see Fig. 15b). These assessments show the feasibility to also exploit such carbonaceous deposit in extremely aggressive chemical environment for the porous Si micropatterning and confirm that a high degree of selectivity can also be achieved in view of optical properties.

This masking effect has also been exploited to block corrosion of iron. Figure 16 shows a SEM image of a carbonaceous micropatterned iron sample after a corrosion test. Clearly, this chemical treatment leads to the selective dissolution of the iron surface resolving the grain structure of the substrate except at the e-beam treated locations. Furthermore, the high degree of protectiveness of EBICD has been

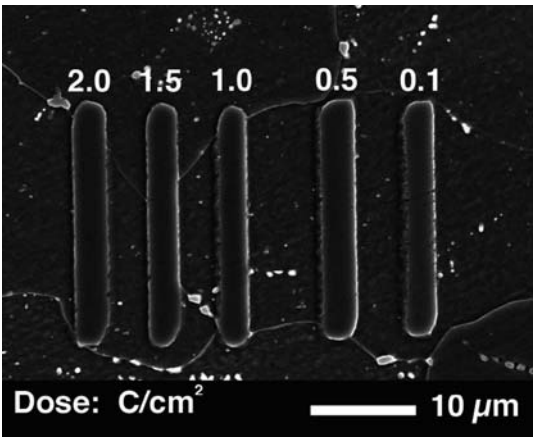

Fig. 16 SEM image showing a patterned iron sample after a corrosion test. (Reproduced by permission of the Electrochemical society, Inc.)

also demonstrated for electrochemical corrosion experiments (see, e.g., Ref. [123]). Thus, this alternative e-beam approach can be used to block a wide range of electrochemical reactions to achieve the patterning of different substrates in the nanometer range.

4 Material Processing by FIB

Focused ion beam (FIB) systems enable the generation of ion beams with diameters of a few nanometers. Similar to SEM, focused ion beam systems enable high-resolution imaging via the detection of secondary electrons or ions generated by the interaction of the energetic ions with target atoms. In comparison to SEMs, the application of heavy ions additionally enables specific material processing with high accuracy. Examples are ion implantation, physical sputtering, ion-beam-induced etching or deposition. Initially intended for maskless implantation of ions, currently focused ion beam systems are mainly used for structuring of sample surfaces by material removal or deposition. Material processing by FIBs is done in a direct writing mode where the ion beam is digitally scanned over the surface of the specimen. In contrast to other structuring techniques mainly based on optical lithography and, therefore, requiring extensive masking, this direct-writing mode makes material processing by FIBs a very flexible and versatile technique successfully applied in many different working areas.

The driving force in the development of focused ion beam systems and their applications is microelectronics. For example, defective masks made for optical lithography can be repaired using FIBs. Excessive material, forming opaque defects, can be removed and missing material can locally be replaced by material deposition [137, 138]. Material processing by focused ion beams also enables the “repair” of integrated circuits. This “rewiring” is mainly used during the development of new

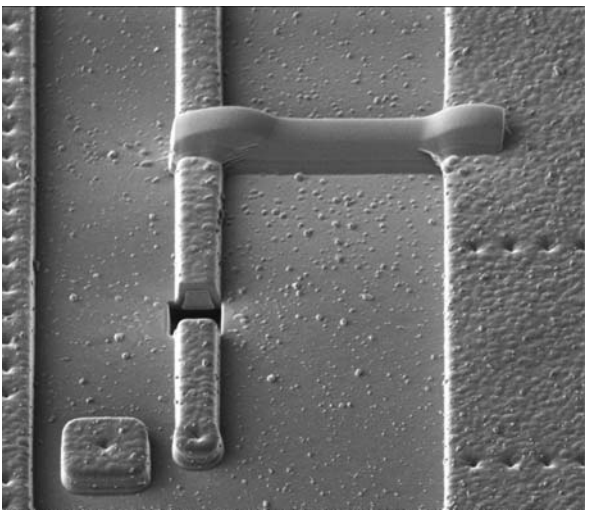

Fig. 17 Modification of an integrated circuit by material processing with focused ion beams. An existing interconnect was cut and a new conductive line was deposited

devices and enables the modification of an integrated circuit by cutting existing interconnects or by creating new conductive lines by material deposition (Fig. 17) [139].

This fast and flexible method replaces extensive and time-consuming fabrication of new prototypes for testing and allows to shorten development time and to decrease costs [140, 141].

In the area of failure analysis, material removal by FIBs is used to prepare cross-sections at definite positions of an integrated circuit and facilitates the optimization of semiconductor processing [142–144]. The capability of high-resolution imaging enables the precise alignment of the cross-section with respect to a special site of the specimen. It also enables the investigation of the cross-section within the same working process. The application of FIBs for the preparation of samples for transmission electron microscopy (TEM) also evolved from microelectronics where TEM is used for the investigation of defects and structures with dimension in the range of nanometers [145–147]. In contrast to conventional preparation techniques, the application of FIBs allows fast fabrication of TEM samples at precisely defined sites without destruction of the specimen as a whole. The extraction of the tiny TEM lamellae from the sample by modern, so-called "lift-out" techniques [148], enables the preparation of TEM lamellae from materials which cannot be processed conventionally. The application of FIBs for the preparation of TEM samples is not restricted to the characterization of semiconductor devices and is nowadays a preparation technique, which is used in many other areas by default.

The ability to fabricate structures with different size and shape in a direct writing mode has created new possibilities and applications in the area of micro- and nanotechnology. Examples are the fabrication of microtools for bio- and medical applications [149, 150] or functionalized probes for scanning probe microscopy (SPM) (Fig. 18) [151, 152].

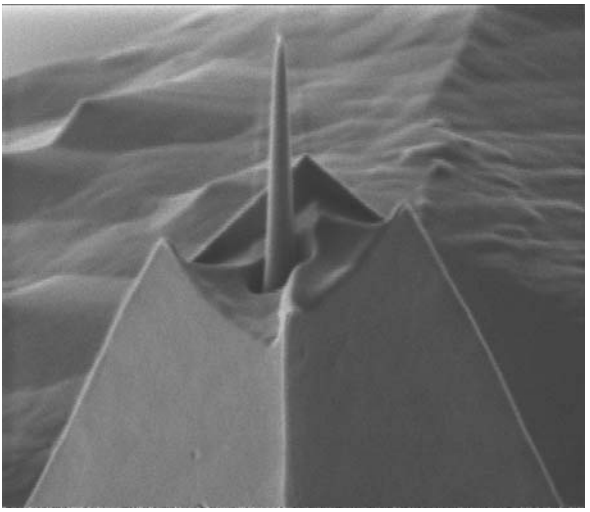

Fig. 18 SEM image of a silicon probe after FIB processing. Physical sputtering was applied to remove material and to create a tip with increased aspect ratio

4.1 Generation of Focused Ion Beams

The first ion-beam columns, dedicated for the generation of focused beams to be applied for material processing, were based on plasma ion sources. By the use of apertures and electrostatic lenses, beam diameters of less than 1 μm could be achieved [153, 154]. Further reduction of beam diameter was possible by the use of ion sources, where the generation of ions is based on the ionization of atoms within an electric field. In comparison to plasma sources, the energy distribution of ions emitted from these so-called field emission sources is clearly reduced. As a result, the beam diameter also decreases as the influence of the chromatic aberration of the ion optics on beam diameter is reduced. The first ion sources based on field ionization were realized by gas emission sources [155]. Because of some drawbacks, for example, low ion currents and technical complexity, gas emission sources nowadays only play a minor role in the generation of FIBs. Today, mainly liquid-metal ion sources are used for the generation of FIBs. This type of ion source was developed in the 1970s and comprises a needle-type emitter, which is wetted by metals or alloys [156]. By heating the emitter above the melting temperature of the metal and simultaneously applying a sufficiently high electrical field between emitter and anode, a variety of elements, for example, Al, As, Ga, Au, B, In, and Li ions can be generated [157]. The element commonly used for the generation of FIBs in commercially available FIB systems is Ga. The requirements that have to be met to generate ions of a definite element with a liquid-metal ion source are low-vapor pressure and high-surface tension of the metal at melting temperature. Additionally, the emitter has to be wetted by the metal, and no chemical reaction should occur between metal and emitter material. Ions from elements with high melting point can only by generated by liquid-metal ion sources, if the element is available in an

alloy with reduced melting point in comparison to the pure element. For sources using alloys, additional mass separation has to be integrated into the ion column, as different ion species are emitted from the ion sources simultaneously.

4.2 Ion Optics

The ion column of a FIB system comprises the ion source and the ion optics. The different components of the ion optics, such as lenses, deflection units, and apertures, are dedicated for the controlled deflection and focusing of the ions after emission from the liquid-metal ion source. Figure 19 schematically shows the main parts of a FIB system.

The liquid-metal ion source is surrounded by a Wehnelt cylinder. This so-called suppressor focuses ions radially emitted from the ion source within a point lying between suppressor and extractor electrode. Between the extractor and the first lens, an electric field is applied, and the ions are accelerated. Because of the high mass of the ions, mainly electrostatic lenses are used for the generation of FIBs. The first lens is used to align the particles relatively to a beam-defining aperture. The diameter of this aperture determines the number of transmitted ions focused on the

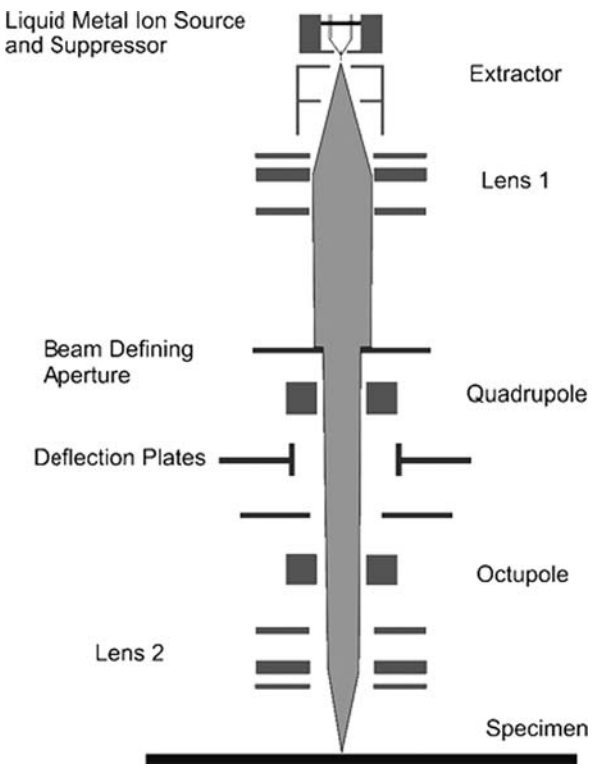

Fig. 19 Schematic showing the main parts of the ion optics of a focused ion beam system

surface of the specimen by the second lens and, therefore, controls the current of the ion beam. Additional electrical components, such as quadrupoles, octupoles, and deflection units, are applied to align the ion beam with respect to the optical axis to make corrections of astigmatism and to scan the ion beam over the sample surface. Currently, commercially available FIB systems mainly use ions with a kinetic energy between 30 keV and 100 keV. Ion-beam currents range from 1 pA to several tens of nA. Presently, the minimum achievable beam diameter (full-width half maximum) is between 5 nm and 7 nm at lowest ion-beam current.

4.3 Material Processing by Focused Ion Beams

Main areas of application of FIBs in the field of material processing are ion implantation, material removal, and material deposition. In addition to physical sputtering, gas-enhanced etching is also used for material removal by ion beams. The combination of energetic ions and etchants, such as iodine-, chlorine-, or fluorine-containing compounds, increases material-removal rates and results in high selectivity. Material deposition is based on the application of dedicated chemical compounds, so-called precursors, which are delivered to the sample surface in a gaseous phase. Due to the co-action of the impinging ions and the precursor molecules adsorbed at the surface of the specimen, different materials, for example, conducting or insulating layers, can be deposited [158].

4.4 Microstructuring by FIB and Electrochemical Reactions

FIB technology has been combined with several electrochemical processes to achieve the microstructuring of surfaces. For instance, it has been reported that aspect ratio of micropatterns can be drastically improved by using FIB etching in macroporous materials [159]. Compared with the aspect ratio obtained by FIB-etched patterns in bulk materials, which is lower than 10, it has been demonstrated that the use of porous silicon fabricated by photoelectrochemistry [160] can be used as a layered structure for the FIB in order to create holes with an overall aspect ratio of 50 (see Fig. 20). This approach has been exploited for the fabrication of 3D silicon photonic crystals and can be also used more generally for the micromachining at a submicrometer scale.

Micromachining can also be performed using the etch stoppers' property of ions-implanted substrates. Indeed, gallium- or boron-implanted areas can act as etch barriers for wet-chemical treatments making this approach useful for the microstructuring of silicon [161–163]. It has been reported that this selective etch behavior can be enhanced when photoelectrochemical etching is carried out on low-doses-implanted species [164]. The etch-barriers effect of implanted species has also been used to selectively etch III–V semiconductors, such as GaAs and InP [165, 166].

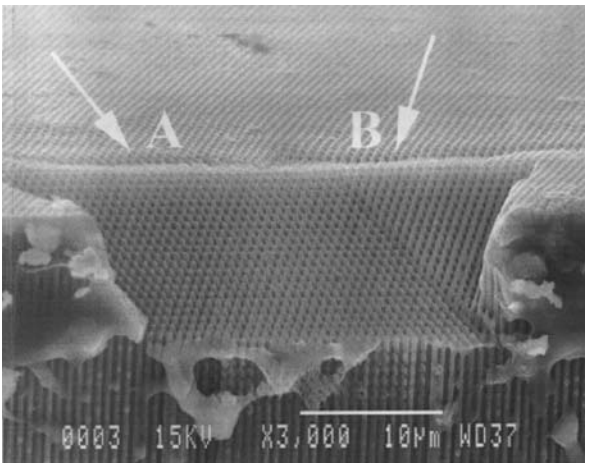

Fig. 20 Yablonovite-like crystal cross-section obtained by ion milling. The FIB etching directions are indicated by *arrows A and B*

The local electrochemical dissolution of implanted areas has also been investigated in order to establish depth profiles of implanted species. This so-called selective electrochemical delineation technique has been studied for the simultaneous electrochemical etching of As- and B-doped silicon substrate as shown in Fig. 21 [167]. This method is extremely sensitive and can be used for production and characterization of devices [168, 169].

Recently, new pathways have been explored to achieve selective electrochemical nanogrowth and nanostructuring of materials on locally sensitized single-crystal semiconductor surfaces. It has been reported how defects intentionally introduced in a surface by FIB bombardment can be used to selectively trigger electrochemical reactions [170–173]. The principle of the approach is based on semiconductor electrochemistry. When electrochemically biased, a semiconductor–electrolyte interface shows a similar electrical characteristic as a metal/semiconductor or p/n junction, that is, a current-passing (accumulation) state when forward biased, a blocking (depletion) state when reverse biased. In the blocking state, a specific "barrier breakdown" $U(\mathrm{Bd})$ potential exists that has been ascribed to the Schottky barrier breakdown of the junction. Due to the current increase at $U(\mathrm{Bd})$, electrochemical reactions are not hampered any longer by insufficient availability of charge carriers and thus can proceed at significant rate. The value of $U(\mathrm{Bd})$ is strongly affected by surface defects, that is, breakdown occurs for much lower applied voltages than for the intact surface. Thus, a processing window for local electrochemical reactions is present between the two threshold potentials $U(\mathrm{Bd})_{\mathrm{intact}}$ and $U(\mathrm{Bd})_{\mathrm{defects}}$ corresponding to the intact and defective surface, respectively. Therefore, by creating locally surface defects, the electrode can be "activated" for an electrochemical reaction only at these surface sites. Figure 22 schematically shows the electrochemical behavior of a p-type semiconductor substrate. The cathodic branch corresponds to the current blocking state, whereas in the anodic branch a passing state is observed. For n-type semiconductors, depletion and accumulation situations are reversed, that

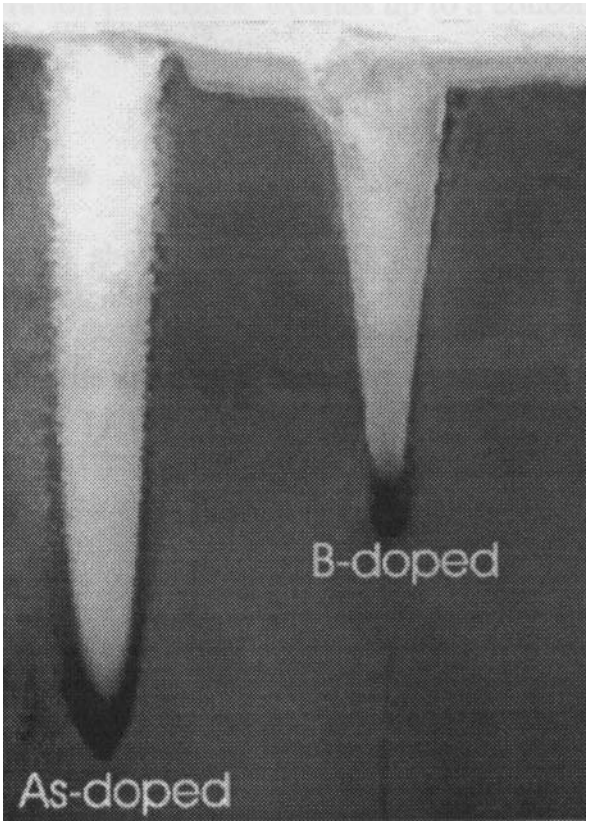

Fig. 21 TEM micrograph showing the simultaneous delineation of As- and B-doped regions after electrochemically etching

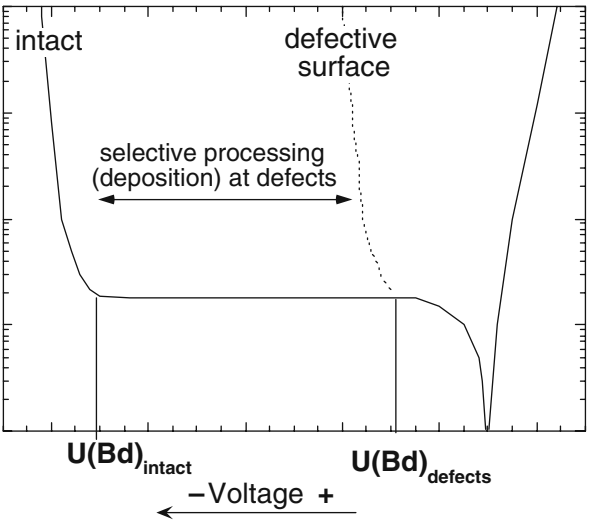

Fig. 22 Schematic current density versus voltage curve for intact and ion-implanted p-Si. Electrodeposition reactions can be initiated selectively between $U(\mathrm{Bd})_{\mathrm{intact}}$ and $U(\mathrm{Bd})_{\mathrm{defects}}$

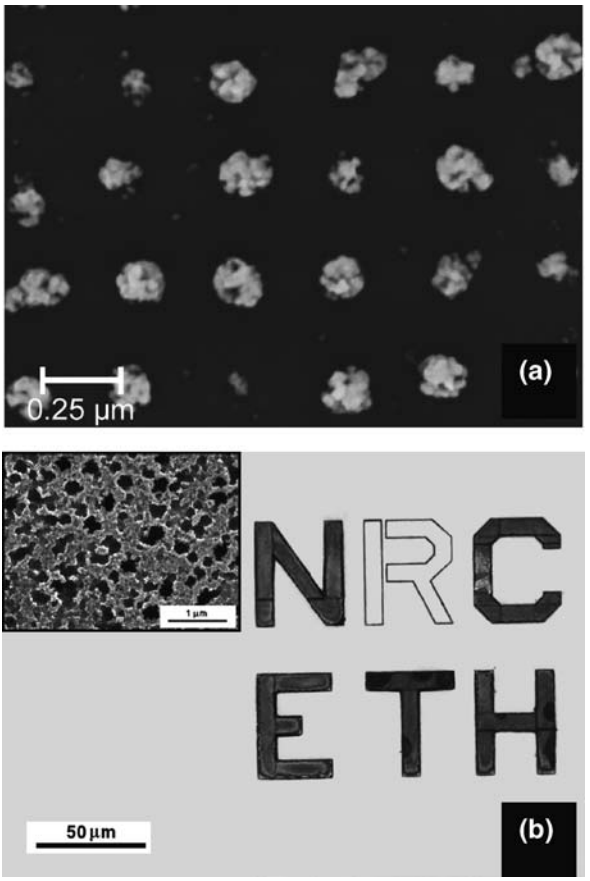

Fig. 23 Examples of selective electrodeposition of gold and electrochemical etching achieved at FIB-induced defects sites

is, current-blocking behavior is observed at anodic potentials and passing behavior at cathodic potentials. Figure 23a shows selective deposition of gold on p-type silicon surface achieved by FIB writing of defect patterns followed by electrochemical deposition of gold performed between $U(\mathrm{Bd})_{\mathrm{intact}}$ and $U(\mathrm{Bd})_{\mathrm{defects}}$. The same approach has been successfully used to form selective light-emitting porous silicon on n-type silicon surface (see Fig. 23b).

References

1. Takumi, U. Sheats, J.R. 1998, X-ray Lithography, J. R. Sheats and B. W. Smith (Ed.), Marcel Dekker, Inc., New York, 403–427.
2. Madou, M. 1997, Fundamentals of microfabrication, CRC Press, Boca Raton.
3. Stockman, L., Heyvaert, I., van Haesendonck, C., and Bruynseraede, Y. 1993, Appl. Phys. Lett., 62, 2935.
4. Matsumoto, K., Ishii, M., Segawa, K., Oka, Y., Vartanian, B.J., and Harris, J.S. 1996, Appl. Phys. Lett., 68, 34.

5. Campbell, P.M., Snow, E.S., and McMarr, P.J. 1995, Appl. Phys. Lett., 66, 1388.
6. Xia, Y. Whitesides, M.W. 1998, Angew. Chem. Int. Ed., 37, 550.
7. Schmuki, P., Maupai, S., Djenizian, T., Santinacci, L., Spiegel, A., and Schlierf, U. 2004, Techniques in Electrochemical Nanotechnology, H. S. Nalwa (Ed.), American Scientific Publishers, Stevenson Ranch, 393–410.
8. Schuster, R., Kirchner, V., Allongue, P., and Ertl, G. 2000, Science, 289, 98.
9. Allongue, P., Jiang, P., Kirchner, V., Trimmer, A.L., and Schuster, R. 2004, J. Phys. Chem. B, 108, 14434.
10. Santinacci, L., Djenizian, T., and Schmuki, P. 2001, Appl. Phys. Lett., 79, 1882.
11. Owen, G. Sheats, J.R. 1998, Electron beam lithography systems, J. R. Sheats and B. W. Smith (Ed.), Marcel Dekker, Inc., New York, 367–401.
12. Stewart, D.K. Casey, J.D.J. 1997, P. Rai-Choudry (Ed.), SPIE Optical Engineering Press, 153.
13. Townsend, P.D., Chandler, P.J., and Zhang, L. 1994, Optical effects of ion implantation, Cambridge University Press, Cambridge.
14. Ryssel, H. Ruge, I. 1986, Ion implantation, John Wiley & Sons
15. Hartley, N.E.W. 1980, Treatise of Materials Science and Tehnology, Academic Press
16. Dearnaley, G. 1982, J. Metals, 34, 18.
17. Straede, C.A. 1989, Wear, 130, 113.
18. Standley, R.D., Gibson, W.M., and Rodgers, J.W. 1972, Appl. Optics, 11, 1313.
19. Heidenreich, R.D. 1964, Fundamentals of Transmission Electron Microscopy, Interscience, New York.
20. Sigmund, P. 1972, Roumaine Phys., 17, 823.
21. Weller, R. 1995, Handbook of Modern ion-Beam Materilas Analysis, J. R. Tessmer & M. Nastasi (Ed.), Materials Research Society, Pittsburg, PA.
22. Nastasi, M.A., Mayer, J.W., and Hirvonen, J.K. 1996, Ion-Solid Interactions, Cambridge University Press.
23. Rutherford, E. 1911, Phil. Mag., 21, 669.
24. Reimer, L. Pfefferkorn, G. 1977, Rasterelektronenmikroskopie, Springer-Verlag Berlin Heidelberg, New York.
25. Werner, U. Johansen, H. 1982, Elektronenmikroskopie in der Festkörperphysik, Springer-Verlag Berlin Heidelberg New York
26. Williams, D.B. Carter, C.B. 1996, Transmission Electron Microscopy I, Plenum Press, New York.
27. Lindhard, J. Scharff, H. 1961, Phys. Rev., 124, 128.
28. Fermi, E. 1928, Z. Phys., 48, 73.
29. Thomas, L.H. 1927, Proc. Cambr. Phil. Soc., 23, 524.
30. Ziegler, J.F., Biersack, J.P., and Littmark, U. 1985, The Stopping and Range of Ions in Solids, Pergamon Press, New York.
31. Lindhard, J. Winter, A. 1964, Mat. -Fys. Medd., 34, N° 4.
32. Bethe, H. 1930, Ann. Phys., 5, 325.
33. Bethe, H. 1932, Z. Phys., 76, 293.
34. Chu, W.K. Powers, D. 1972, Phys. Lett., 40A, 23.
35. Kramers, M.A. 1923, Phil. Mag., 46, 836.
36. Hobbs, L.W. 1979, Introduction to Analytical Electron Microscopy, J. I. Goldstein & D. C. Joy J. J. Hren (Ed.), Plenum Press New York, 437.
37. Kinchin, G.H. Pease, R.S. 1955, Rep. Prog. Phys., 18, 1.
38. Sigmund, P. 1969, Phys. Rev., 184, 383.
39. Matsunami, N., Yamamura, Y., Itikawa, Y., Itoh, N., Kazumata, Y., Miyagawa, S., Morita, K., Shimizu, R., and Tawara, H. 1984, At. Data Nucl. Data Tables, 31, 1.
40. Smith, K.C.A. Oatley, C.W. 1955, Br. J. Appl. Phys., 6, 391.
41. Buck, D.A. Shoulders, K. 1957, in Proceedings Eastern Joint Computer Conference, ATEE, New York, 55.

42. Broers, A.N. 1965, Microelectron. Reliab., 4, 103.
43. Craighead, H.G., Howard, R.E., Jackel, L.D., and Mankiewich, P.M. 1983, Appl. Phys. Lett., 42, 38.
44. Sedgwick, T.O., Broers, A.N., and Agule, B.J. 1972, J. Electrochem. Soc., 119, 1769.
45. Broers, A.N., Molzen, W.W., Cuomo, J.J., and Wittels, N.D. 1976, Appl. Phys. Lett., 29, 596.
46. Rakhshandehroo, M.R. Pang, S.W. 1996, J. Vac. Sci. Technol. B, 14, 612.
47. Sung, K.T. Pang, S.W. 1992, J. Vac. Sci. Technol. B, 10, 2211.
48. Simon, G., Haghiri Gosnet, A.M., Carcenac, F., and Launois, H. 1997, Microelectron. Eng., 35, 51.
49. Allee, D.R., Umbach, C.P., and Broers, A.N. 1991, J. Vac. Sci. Technol. B, 9, 2838.
50. Matsui, S., Ichihashi, T., and Mito, M. 1989, J. Vac. Sci. Technol. B, 7, 1182.
51. Allee, D.R. Broers, A. 1990, Appl. Phys. Lett., 57, 2271.
52. Pan, X., Allee, D.R., Broers, A., Tang, Y.S., and Wilkinson, C.W. 1991, Appl. Phys. Lett., 59, 3157.
53. Jackel, L.D., Howard, R.E., Mankiewich, P.M., Craighead, H.G., and Epworth, W. 1984, Appl. Phys. Lett., 45, 698.
54. Schmoranzer, H. 1988, J. Vac. Sci. Technol. B, 6, 2053.
55. Parikh, M. Kyser, D.F. 1979, J. Appl. Phys., 50, 1004.
56. Chang, T.H.P. 1975, J. Vac. Sci. Technol., 12, 1271.
57. Haller, I., Hatzakis, M., and Srinivassan, R. 1968, IBM J. Res. Dev., 251.
58. Thomson, L.F., Stillwagon, L.E., and Doerries, E.M. 1978, J. Vac. Sci. Technol., 15, 938.
59. Dobisz, E.A., Marrian, C.R.K., and Colton, R.J. 1991, J. Appl. Phys., 70, 1793.
60. Gölzhäuser, A., Geyer, W., Stadler, V., Eck, W., Grunze, M., Edinger, K., Weimann, T., and Hinze, P. 2000, J. Vac. Sci. Technol. B, 18, 3414.
61. Lercel, M.J., Craighead, H.G., Parikh, A.N., Seshadri, K., and Allara, D.L. 1996, Appl. Phys. Lett., 68, 1504.
62. Fujita, J., Watanabe, H., Ochiai, Y., Manako, S., Tsai, J.S., and Matsui, S. 1995, J. Vac. Sci. Technol. B, 13, 2757.
63. Muray, A., Scheinfein, M., Isaacson, M., and Adesida, I. 1985, J. Vac. Sci. Technol. B, 3, 367.
64. Thackeray, J.W., Orsula, G.W., Canistro, D., and Berry, A.K. 1989, J. Photopolymer Sci. Technol., 2, 429.
65. Scherer, A. Craighead, H.G. 1987, J. Vac. Sci. Technol. B, 5, 374.
66. Broers, A.N. 1988, IBM J. Res. Dev., 32, 502.
67. Eigler, D.M. Schweizer, E.I. 1991, Nature, 344, 524.
68. Umbach, C.P., Washburn, S., Laibowitz, R.B., and Webb, R.A. 1984, Phys. Rev. B, 30, 4048.
69. Xu, W., Wong, J., Cheng, C.C., Johnson, R., and Scherer, A. 1995, J. Vac. Sci. Technol. B, 13, 2372.
70. Chen, Y.L., Chen, C.C., Jeng, J.C., and Chen, Y.F. 2004, Appl. Phys. Lett., 85, 1259.
71. Dubois, S., Duvail, J.L., and Piraux, L. 2000, Actual. Chimique, 4, 42.
72. Li, A.P., Müller, F., and Gösele, U. 2000, Electrochem. and Solid-State Lett., 3, 131.
73. Borini, S., Amato, G., Rocchia, M., Boarino, L., and Rossi, A.M. 2003, J. Appl. Phys., 93, 4439.
74. Borini, S. 2005, J. Electrochem. Soc., 152, G482.
75. Ulman, R. 1996, Chem. Rev., 96, 1533.
76. Ulman, A. 1991, An Introduction to Ultrathin Organic Films From Langmuir-Blodgett to Self-Assembly, Academic press, Inc., San Diego.
77. Effenberger, F., Goetz, G., Bidlingmaier, B., and Wezstein, M. 1998, Angew. Chem., 110/18, 2651.
78. Effenberger, F., Goetz, G., Bidlingmaier, B., and Wezstein, M. 1998, Angew. Chem. Int. Ed., 37, 2462.
79. Linford, M.R. Chidsey, C.E.D. 1993, J. Am. Chem. Soc., 115, 12631.

80. Boukherroub, R., Morin, S., Sharpe, P., Wayner, D.D.M., and Allongue, P. 2000, Langmuir, 16, 7429.
81. White, H.S., Kittlesen, G.P., and Wrighton, M.S. 1984, J. Am. Chem. Soc., 106, 5375.
82. Chidsey, C.E.D. 1991, Science, 251, 219.
83. Frisbie, C.D., Fritsch-Faules, I., Wollman, E.W., and Wrighton, M.S. 2002, Thin-Solid-Films, 210, 341.
84. Chaki, N.K. Vijayamohanan, K. 2002, Biosens. Bioelectron., 17, 1.
85. Dulcey, C.S., Georger, J.H., Krauthamer, V., Stenger, D.A., Fare, T.L., and Calver, M.J. 1991, Science, 252, 551.
86. Perkins, M.K., Dobisz, E.A., Brandow, S.L., Calvert, J.M., Kosakowski, J.E., and Marrian, C.R.K. 1996, Appl. Phys. Lett., 68, 550.
87. Ada, E.T., Hanley, L., Etchin, S., Melngailis, J., Dressick, W.J., Chen, M.S., and Calvert, J.M. 1995, J. Vac. Sci. Technol. B, 13, 2189.
88. Lercel, M.J., Whelan, C.S., Craighead, H.G., Seshadri, K., and Allara, D.L. J. Vac. Sci. Technol. B, 14, 4085.
89. Sondag Huethorst, J.A.M., van Helleputte, H.R.J., and Fokkink, L.G.J. 1994, Appl. Phys. Lett., 64, 285.
90. Koops, H.W.P., Schössler, C., Kaya, A., and Weber, M. 1996, J. Vac. Sci. Technol. B, 14, 4105.
91. Fritzsche, W., Kohler, J.M., Bohm, K.J., Unger, E., Wagner, T., Kirsch, R., Mertig, M., and Pompe, W. 1999, Nanotechnology, 10, 331.
92. Kohlmann von Platen, K.T., Thiemann, M., and Brünger, W.H. 1991, Microelectron. Eng., 13, 279.
93. Koops, H.W.P. 1996, T. C. Hale and K. L. Telschow (Ed.), Proceedings of SPIE Volume, 248.
94. Koops, H.W.P., Munro, E., Rouse, J., Kretz, J., Rudolph, M., Weber, M., and Dahm, G. 1995, Nucl. Instrum. Methods Phys. Res. B, 363, 1.
95. Weber, M., Rudolph, M., Kretz, J., and Koops, H.W.P. 1995, J. Vac. Sci. Technol. B, 13, 461.
96. Schoessler, C. Koops, H.W.P. 1998, J. Vac. Sci. Technol. B, 16, 862.
97. Koops, H.W.P., Kretz, J., Rudolph, M., and Weber, M. 1993, J. Vac. Sci. Technol. B, 11, 2386.
98. Voss, R.F., Laibowitz, R.B., and Broers, A.N. 1980, Appl. Phys. Lett., 37, 656.
99. Komuro, M. Hiroshima, H. 1997, Microelectron. Eng., 35, 273.
100. Matsui, S. Mori, K. 1986, J. Vac. Sci. Technol. B, 4, 299.
101. Utke, I., Luisier, A., Hoffmann, P., Laub, D., and Buffat, P.A. 2002, Appl. Phys. Lett., 81, 3245.
102. Hübner, U., Plontke, R., Blume, M., Reinhardt, A., and Koops, H.W.P. 2001, Microelectron. Eng., 57, 953.
103. Christy, R.W. 1960, J. Appl. Phys., 31, 1680.
104. Koops, H., Weiel, R., Kern, D.P., and Baum, T.H. 1988, J. Vac. Sci. Technol. B, 6, 477.
105. Scheuer, V., Koops, H., and Tschudi, T. 1986, Microelectron. Eng., 5, 423.
106. Hoyle, P.C., Ogasawara, M., and Cleaver, J.R.A. 1993, Appl. Phys. Lett., 62, 3043.
107. Reimer, L. 1997, Transmission Electron Microscopy, Springer-Verlag, Berlin.
108. Lee, K.L. Hatzakis, M. 1989, J. Vac. Sci. Technol. B, 7, 941.
109. Hoyle, P.C., Cleaver, J.R.A., and Ahmed, H. 1994, Appl. Phys. Lett., 64, 1448.
110. Kuntz, R.R. Mayer, T.M. 1986, J. Vac. Sci. Technol. B, 5, 427.
111. Miura, N., Ishii, H., Shirakashi, J., Yamada, A., and Konagai, M. 1997, Appl. Surf. Sci., 113/114, 269.
112. Miura, N., Numaguchi, T., Yamada, A., Konagai, M., and Shirakashi, J.I. 1997, Jpn. J. Appl. Phys., 36, 1619.
113. Miura, N., Ishii, H., Yamada, A., and Konagi, M. 1996, Jpn. J. Appl. Phys., 35, L1089.
114. Amman, M., Sleight, J.W., Lombardi, D.R., Welser, R.E., Deshpande, M.R., Reed, M.A., and Guido, L.J. 1996, J. Vac. Sci. Technol. B, 14, 54.

115. Guise, O., Ahner, J., Yates Jr, J.T., and Levy, J. 2004, Appl. Phys. Lett., 85, 2352.
116. Zeng, Z.M., Tian, X.B., Kwok, T.K., Tang, B.Y., Fung, M.K., and Chu, O.K. 2000, J. Vac. Sci. Technol. A, 18, 2164.
117. Zhang, S., Zeng, X.T., Xie, H., and Hing, P. 2000, Surf. Coat. Technol., 123, 256.
118. Broers, A.N. 1964, in Proceedings of the First International Conference on Electron and Ion Beam Technology, Wiley, New York, 181.
119. Molzen, W.W., Broers, A.N., Cuomo, J.J., Harper, J.M.E., and Laibowitz, R.B. 1979, J. Vac. Sci. Technol., 16, 269.
120. Ueta, A., Avramescu, A., Uesugi, K., Suemune, I., Machida, H., and Shimoyama, N. 1998, Jpn. J. Appl. Phys., 37, 272.
121. Djenizian, T., Santinacci, L., and Schmuki, P. 2001, Appl. Phys. Lett., 78, 2840.
122. Miura, N., Yamada, A., and Konagai, M. 1997, Jpn. J. Appl. Phys., 36, L1275.
123. Sieber, I., Hildebrand, H., Djenizian, T., and Schmuki, P. 2003, Electrochem. and Solid-State Lett., 6, C1.
124. Djenizian, T., Macak, J., and Schmuki, P. 2002, in Nano- and Micro-Electromechanical Systems (NEMS and MEMS) and Molecular Machines, Mat. Res. Soc. Symp. Proc., Boston, 79–83.
125. Djenizian, T., Santinacci, L., and Schmuki, P. 2001, J. Electrochem. Soc., 148, 197.
126. Scharifker, B. Hills, G. 1983, Electrochim. Acta, 28, 879.
127. Scharifker, B. Mostany, J. 1984, J. Electroanal. Chem., 177, 13.
128. Gunawardena, G., Hills, G., Montenegro, I., and Scharifker, B. 1982, J. Electroanal. Chem., 138, 225.
129. Scherb, G. Kolb, D.M. 1995, J. Electroanal. Chem., 396, 151.
130. Vereecken, P.M., Strubbe, K., and Gomes, W.P. 1997, J. Electroanal. Chem., 433, 19.
131. Stiger, R.M., Gorer, S., Craft, B., and Penner, R.M. 1999, Langmuir, 15, 790.
132. Oskam, G., van Heerden, D., and Searson, P.C. 1998, Appl. Phys. Lett., 73, 3241.
133. Pasa, A.A. Schwarzacher, W. 1999, Phys. Status Solidi A, 173, 73.
134. Rashkova, B., Guel, B., Pötzschke, R.T., Staikov, G., and Lorenz, W.J. 1998, Electrochim. Acta, 43, 3021.
135. Djenizian, T., Santinacci, L., and Schmuki, P. 2004, J. Electrochem. Soc., 151, G175-G180.
136. Djenizian, T., Santinacci, L., Hildebrand, H., and Schmuki, P. 2003, Surf. Sci., 524, 40.
137. Stewart, D.K., Doyle, A.F., and Casey, J.D.J. 1995, SPIE, 2437, 276.
138. Xu, X. Melngailis, J. 1993, J. Vac. Sci. Technol. B, 11, 2436.
139. Frey, L. Lehrer, C. 2003, Praktische Metallographie, 40, 184.
140. Hooghan, K.N., Wills, K.S., Rodriguez, P.A., and O′Connell, S. 1999, in ASM International, Materials Park, Ohio, 247.
141. Van Doorselaer, K., Van den Reeck, M., Van Den Bempt, L., Young, R., and Whitney, J. 1993, in Proc. 19th International Symposium for Testing and Failure Analysis, ASM International, Materials Park, Ohio, 405.
142. Verkleij, D. 1998, Microelectron. Reliab., 38, 869.
143. Nikawa, K. 1994, IEICE Trans. Fund. Electr., E77, 174.
144. Hahn, L.L., Abramo, M.T., and Coutu, P.T. 1991, in Proc. 17th International Symposium for Testing and Failure Analysis, ASM International, Materials Park, Ohio, 1.
145. Walker, J.F., Reiner, J.C., and Solenthaler, C. 1995, Inst. Phys. Conf. Ser., 146, 629.
146. Ishitani, T. Yaguchi, T. 1996, Microsc. Res. Techn., 35, 320.
147. Rai, R., Subramanian, S., Rose, S., Conner, J., Schani, P., and Moss, J. 2000, in Proc. 26th International Symposium for Testing and Failure Analysis, 415.
148. Stevie, F.A., Irwin, R.B., Shofner, T.L., Brown, S.R., Drown, J.L., and Giannuzzi, L.A. 1998, in, American Institute of Physics, Woodburry, NY, 868.
149. Vasile, M.J., Xie, J., and Nassar, R. 1999, J. Vac. Sci. Technol. B, 17, 3085.
150. Ishitani, T., Ohnishi, T., Madokoro, Y., and Kawanami, Y. 1991, J. Vac. Sci. Technol. B, 9, 2633.

151. Vasile, M.J., Grigg, D., Griffith, J.E., Fitzgerald, E., and Russel, P.E. 1991, J. Vac. Sci. Technol. B, 9, 3569.
152. Olbrich, A., Ebersberger, B., Boit, C., Niedermann, P., Hänni, W., Vancea, J., and Hoffmann, H. 1999, J. Vac. Sci. Technol. B, 17, 1570.
153. Hill, A.R. 1968, Nature, 218, 292.
154. Guharay, S.K., E., S., and Orloff, J. 1999, J. Vac. Sci. Technol. B, 17, 2779.
155. Orloff, J. Swanson, L.W. 1975, J. Vac. Sci. Technol. B, 12, 1209.
156. Kohn, V.E. Ring, G.R. 1975, Appl. Phys. Lett., 27, 479.
157. Orloff, J. 1993, Rev. Sci. Instrum., 64, 1105.
158. Frey, L. Lehrer, C. 2003, Applied Physics A, 76, 1017.
159. Wang, K., Chelnokov, A., Rowson, S., Garoche, P., and Lourtioz, J.M. 2000, J. Phys. D: Appl. Phys., 33, L119.
160. Gruning, U., Lehmann, V., Ottow, S., and Bush, K. 1996, Appl. Phys. Lett., 68, 747.
161. Schmidt, B., Bischoff, L., and Teichert, J. 1997, Sens. Actuators A, 61, 369.
162. Brugger, J., Beljakovic, G., Despont, M., de Rooiji, N.F., and Vettiger, P. 1997, Microelectron. Eng., 35, 401.
163. Chen, W., Chen, P., Madhukar, R., Viswanathan, R., and So, J. 1993, Mater. Res. Soc. Proc., 279, 599.
164. Cummings, K.D., Harriott, L.R., Chi, G.C., and Ostermayer, F.W. 1986, Proc. SPIE Int. Soc. Opt. Eng., 93.
165. Arimoto, H., Kosugi, M., Kitada, H., and Miyauchi, E. 1989, Microelectron. Eng., 9, 321.
166. Rennon, S., Bach, L., König, H., Reithmaier, J.P., Forchel, A., Gentner, J.L., and Goldstein, L. 2001, 57–58, 891.
167. D′Arrigo, G. Spinella, C. 2001, Mater. Sci. Semicond. Proc., 4, 93.
168. Spinella, C. 1998, Mater. Sci. Semicond. Proc., 1, 55.
169. Garozzo, G., La Magna, A., Coffa, S., D′Arrigo, G., Parasole, N., Renna, M., and Spinella, C. 2002, Comp. Mater. Sci., 24, 246.
170. Schmuki, P., Erickson, L.E., and Lockwood, D.J. 1998, Phys. Rev. Lett., 80, 4060.
171. Schmuki, P. Erickson, L.E. 2000, Phys. Rev. Lett., 85, 2985.
172. Spiegel, A., Erickson, L.E., and Schmuki, P. 2000, J. Electrochem. Soc., 147, 2993.
173. Spiegel, A., Staemmler, L., Dobeli, M., and Schmuki, P. 2002, J. Electrochem. Soc., 149, C432.
174. Berger, M.J. and Seltzer, S.M. 1964, NASA-SP-3012.
175. Fitting, H.J. 1974, Phys. Stat. Sol. A, 26, 525.
176. Gibbons, J.F., Johnson, W.S., and Mylroie, S.W. 1975, Projected Range Statistics, Stroudsburg.